Estimation of the Sarcoplasmic Reticulum Ca^{2+} Release Flux Underlying Ca^{2+} Sparks

Christian Soeller and Mark B. Cannell
Department of Physiology, University of Auckland School of Medicine, Grafton, Auckland 1, New Zealand

ABSTRACT Using a combination of experimental and numerical approaches, we have tested two different approaches to calculating the sarcoplasmic reticulum (SR) Ca^{2+} release flux, which gives rise to cardiac muscle Ca^{2+} sparks. By using two-photon excited spot photolysis of DM-Nitrophen, known Ca^{2+} release flux time courses were generated to provide the first experimental validation of spark flux reconstruction algorithms. These artificial Ca^{2+} sparks show that it is possible to calculate the SR Ca^{2+} release waveform with reasonable accuracy, provided the flux equations reasonably reflect the properties of the experimental system. Within cardiac muscle cells, we show that Ca^{2+} flux reconstruction is complicated by the substantial dye binding to proteins, a factor that has not been adequately addressed in previous flux reconstruction algorithms. Furthermore, our numerical experiments suggest that the calculated time course of release flux inactivation based on conventional flux reconstruction algorithms is likely to be in error. We therefore developed novel algorithms based on an explicit dye binding scheme. When these algorithm were applied to evoked Ca^{2+} sparks in rat cardiac ventricular myocytes, the reconstructed Ca^{2+} release waveform peaked in ~5 ms and decayed with a halftime of ~5 ms. The peak flux magnitude was 7–12 pA, suggesting that sparks must arise from clusters of >15 ryanodine receptors.

INTRODUCTION

Transient microscopic elevations in cytosolic Ca^{2+} concentration, termed "Ca^{2+} sparks," were first discovered in ventricular cardiac muscle cells labeled with the Ca^{2+}-sensitive indicator dye fluo-3 (Cheng et al., 1993). Subsequently, Ca^{2+} sparks were also observed in other striated and smooth muscle cells (Tsugorka et al., 1995; Klein et al., 1996). The spatio-temporal summation of individual Ca^{2+} sparks can explain the cell-wide Ca^{2+} transient during activation of cardiac muscle cells (Cannell et al., 1994; Bridge et al., 1999). Ca^{2+} sparks occur at the location of t-tubules (Shacklock et al., 1995; Cheng et al., 1996a), which is where the dyadic junctions between closely opposed transverse tubular and sarcoplasmic reticulum (SR) membranes occur (Jorgensen et al., 1993; Soeller and Cannell, 1997; Franzini-Armstrong et al., 1999). The discovery of these local events has helped to explain how cardiac excitation–contraction coupling can exhibit high amplification of the trigger Ca^{2+} influx across the sarcolemma without becoming unstable (Stern, 1992; Cannell et al., 1995; Santana et al., 1996).

Recent studies suggest that cardiac Ca^{2+} sparks arise from the opening of a small number of SR release channels or ryanodine receptors (RyRs) (Bridge et al., 1999; Lukyanenko et al., 2000; Wang et al., 2001). Because the fluorescence image of a Ca^{2+} spark reflects the gating of RyRs in their native environment, analysis of Ca^{2+} sparks can provide insight into the regulation and gating of RyRs in situ. The magnitude of the SR Ca^{2+} release flux underlying Ca^{2+} sparks is the product of the number of RyRs present, their single-channel flux, and their open probability and can be used to provide insight into these variables (Cannell and Soeller, 1998). For example, if just the single-channel current is known, the minimum number of RyRs involved in generating a Ca^{2+} spark can be estimated. If the number of channels is also known (for a fixed spark site under steady-state conditions), the open probability of the RyRs can be estimated.

Unfortunately, extraction of the Ca^{2+} release flux underlying Ca^{2+} sparks is complicated by the recorded fluorescence transient not being a direct measure of the SR release flux. This problem arises from the diffusion and binding of Ca^{2+} to the indicator (and other Ca^{2+} binding species) and the low signal-to-noise ratio of the recorded Ca^{2+} spark. Although flux reconstruction methods have been used to estimate SR release fluxes underlying sparks (Blatter et al., 1997; Rios et al., 1999) and analyze modulation of RyR gating (Lukyanenko et al., 1998), a number of serious problems and uncertainties remain. First, the ability to extract the release flux underlying Ca^{2+} sparks has not yet been experimentally tested. Second, it is known that significant dye binding to immobile structures occurs in the cytosol (Harkins et al., 1993) and a recent study of Ca^{2+}-indicator signals from muscle has shown that a detailed model of indicator binding is required to explain the experimental observations (Hollingworth et al., 2000). Nevertheless, all previous reconstruction procedures have been based on "simple" dye binding models where the binding of the fluorescent indicator dye to immobile intracellular structures was not considered in detail (but approximated using a lower effective diffusion coefficient). A third problem arises from the sensitivity of the flux reconstruction algo-

Submitted August 17, 2001, and accepted for publication February 11, 2002.

Address reprint requests to C. Soeller, Dept. of Physiology, Univ. of Auckland School of Medicine, Private Bag 92019, Auckland 1, New Zealand. Tel.: +64-9-373-7599; Fax: +64-9-373-7499; E-mail: c.soeller@auckland.ac.nz.

0006-3495/02/05/2396/19 $2.00

TABLE 1 Fluo-3 binding constants

Reaction	On Rate Symbol	On Rate (10^8 $M^{-1}s^{-1}$)	Off Rate Symbol	Off Rate (s^{-1})	Dissociation Constant (μM)
Ca^{2+} + F3 ⇔ F3Ca	k_{on}^{F3}	3.5	k_{off}^{F3}	177.5	0.51
Ca^{2+} + PF3 ⇔ PF3Ca	k_{off}^{PF3}	0.225	k_{off}^{PF3}	43.0	1.91
F3 + P ⇔ PF3	k_{on}^{P}	0.15	k_{off}^{P}	5.5×10^3	367.00
F3Ca + P ⇔ PF3Ca	k_{on}^{PCa}	0.15	k_{off}^{PCa}	2.07×10^4	1380.00

Parameters of the Harkins scheme. Values were adjusted from 16 to 22°C assuming a Q_{10} of 2.0. Total fluo-3 concentration in simulations and reconstructions was 100 μM. The total concentration of fluo-3 binding sites on protein (P) was set to 3 mM. This results in 87% of fluo-3 bound to protein at a resting [Ca^{2+}] of 100 nm (cf. Zhao et al., 1996).

rithm to noise in the input data, which, in combination with the noise associated with Ca^{2+} sparks records, renders estimation of release fluxes problematic. Although averaging of Ca^{2+} spark records could provide a way to improve the signal-to-noise ratio of the input data, simply averaging from randomly selected sites is complicated by the site-to-site variation in Ca^{2+} spark properties (Parker and Wier, 1997; Bridge et al., 1999). Finally, it is unknown whether the average reconstructed release flux is proportional to the release flux reconstructed from an averaged Ca^{2+} spark (i.e., if the method is linear). Without such linearity, the flux reconstructed from average sparks will not reflect the flux underlying individual Ca^{2+} sparks.

In this study, we have tested some of the implicit assumptions of previous flux reconstruction methods and have developed new methods that are applied to sparks recorded with an averaging protocol. By generating artificial Ca^{2+} sparks with known underlying fluxes (with two-photon excited spot photolysis of caged Ca^{2+}, Soeller and Cannell, 1999b) we have obtained the first experimental test of a flux reconstruction method. In addition, we have investigated how a more complicated dye binding model (Harkins et al., 1993) improves flux estimation. Our results highlight the errors associated with an oversimplification of the processes shaping the Ca^{2+} spark and suggest that the calculated time course of release flux inactivation based on the conventional flux reconstruction algorithm (Lukyanenko et al., 1998) is in error (because it depends on the amplitude of release flux). Our spark reconstructions calculated with the new algorithm suggest peak fluxes of 7–12 pA, suggesting that sparks must arise from clusters of >15 RyRs. Some of these results have been presented in abstract form (Soeller and Cannell, 2001).

METHODS

Numerical modeling

A numerical model of Ca^{2+} sparks was used to generate simulated fluorescence data for some numerical tests of the flux reconstruction algorithms. To accurately model the binding of the fluorescent indicator fluo-3 to Ca^{2+} and proteins (Hollingworth et al., 2000), the scheme suggested by Harkins et al. (1993) was used. This scheme accounts for dye binding to immobile structures and the reduced apparent Ca^{2+} affinity of fluo-3 that is observed in intact cells. Figure 3 *A* shows the binding scheme, and the various on- and off-rates are summarized in Table 1 (adjusted from 16°C to 22°C using a Q_{10} of 2, cf. Hollingworth et al., 2000). Only the protein-free fluo-3 (F3) and fluo-3-Ca complex (F3Ca) are free to diffuse in this scheme. The value of the free diffusion coefficient (D_{F3}) was estimated from published values of the diffusion coefficients of fluorescein and rhodamine 6G in water at 25°C (5.1 and $2.8 \cdot 10^{-6}$ cm^2/s, respectively, (Ko et al., 1997)). Assuming approximate spherical symmetry of the diffusing molecules and a van der Waals volume directly proportional to molecular weight (Ko et al., 1997) fluo-3 should be 1.37 and 1.2 times larger than fluorescein and rhodamine 6G, respectively. Thus, D_{F3} should lie between 2.3 and $3.7 \cdot 10^{-6}$ cm^2/s in water. We therefore assumed a value of $3 \cdot 10^{-6}$ cm^2/s for diffusion in water. Because the viscosity of the cytosol is approximately twice that of a simple salt solution (Kushmerick and Podolsky, 1969) a value of $1.5 \cdot 10^{-6}$ cm^2/s was used for modeling and flux reconstruction in cell experiments. The resulting reaction–diffusion equations for the fluo-3-Ca complex (free and protein bound) are listed in the Appendix (Eqs. A1 and A2), and corresponding equations describe the evolution of Ca^{2+} free fluo-3 concentration.

The reaction diffusion equation for Ca^{2+} is given in Eq. A5 in the Appendix. Binding to various Ca^{2+} buffers in the cytosol gives rise to a flux q_{buf} (Eq. A6), SR uptake causes an additional removal flux (q_{rem}) and the principal source of Ca^{2+} influx is the Ca^{2+} release flux (q_{Ca}). With first-order buffer reactions,

$$B_i + Ca^{2+} \underset{k_{on}^{i}}{\overset{k_{off}^{i}}{\Leftrightarrow}} B_iCa.$$

Immobile buffers included troponin and Ca^{2+} binding sites on the outer SR membrane and the inner sarcolemma. Membrane binding sites were treated as homogeneously distributed throughout the cytosol (Smith et al., 1998). Diffusible buffers included adenosine triphosphate and calmodulin. As previously used in a model of Ca^{2+} movements in skeletal muscle (Baylor and Hollingworth, 1998), we used effective adenosine triphosphate Ca^{2+} binding rates in the presence of 0.5 mM Mg^{2+} to reduce the number of differential equations (i.e., we assume constant [Mg^{2+}]). Binding rates, total concentrations and diffusion coefficients for the various species (with references) are given in Table 2.

SR uptake was approximated according to the equation,

$$q_{rem} = \frac{k_{SR,max}[Ca^{2+}]^m}{K_{D,SR}^m + [Ca^{2+}]^m}, \quad (1)$$

where $k_{SR,max}$ is $2 \cdot 10^{-4}$ Ms^{-1}, m is 3.9 and $K_{D,SR}$ is 184 nM (Bassani et al., 1994). Strictly speaking, a SR leak that matches the uptake activity at resting [Ca^{2+}] should be included. However, this flux was so small that we could neglect it on the time scale of these simulations (<30 ms).

The Ca^{2+} release flux q_{Ca} time course was either a step lasting for 10 ms or an exponentially decaying function with a time constant of 7 ms. The amplitude of the release flux was varied between 0.5 and 16.5 pA (see

TABLE 2 Endogenous Ca^{2+} buffers

Buffer Species	k_{on} (10^8 $M^{-1}s^{-1}$)	k_{off} (s^{-1})	Conc (μM)	D (10^{-6} cm^2s^{-1})	Reference
Troponin-C	0.39	20	70		Sipido and Wier, 1991
SR (outer sites)	1.15	100	47		Balke et al., 1994
SL (inner sites)	1.15	1×10^3	1124		Balke et al., 1994
Calmodulin	1.0	38	24	4.2×10^{-3}	Sipido and Wier, 1991 Luby-Phelps et al., 1995
ATP	0.137	3×10^4	8×10^3	1.4	Baylor and Hollingworth, 1998

Results). The release flux was spread uniformly over a spherical region 200 nm in radius resembling the diameter of junctional diads in cardiac muscle (see Langer and Peskoff, 1996; Soeller and Cannell, 1997).

The Ca^{2+} diffusion coefficient in the cytosol (D_{Ca}) was $3 \cdot 10^{-6}$ cm^2s^{-1} to account for the higher viscosity of the cytosol as compared to simple salt solutions (Kushmerick and Podolsky, 1969). All simulations were started from a uniform equilibrium distribution of all species at a resting Ca^{2+} concentration of 100 nM. The model equations were implemented using FACSIMILE (Chance et al., 1977) on a uniform grid with spherical symmetry. The radius of the simulation space was 10 μm, with a grid spacing of 67 nm.

Simulation of line scan images

Protein-bound and protein-free forms of the Ca-fluo-3 complex were assumed to contribute equally to emitted fluorescence (Harkins et al., 1993). The contribution of Ca^{2+}-free fluo-3 to measured fluorescence was neglected because it fluoresces about 200 times less strongly than Ca-fluo-3 (Harkins et al., 1993). Records of normalized fluorescence (F/F_0) were generated by dividing the computed distribution of total fluo-3-Ca complex ([TF3Ca], see Eq. A3) by the equilibrium value calculated at the resting [Ca^{2+}]. Optical blurring by a confocal microscope was simulated by convolving the calculated fluorescence distribution with a point spread function (PSF) that was the product of Gaussians in x, y, and z directions, respectively (where z was chosen parallel to the optical axis). Gaussians with a full width at half maximum (FWHM) of 0.4 μm in x and y and 0.9 μm in z were chosen to mimic the resolution that we routinely achieve in experiments (as measured with subresolution fluorescent beads). Finally, line scan images (Cannell et al., 1994) were simulated by extracting the time course of blurred and normalized fluorescence along a line located at a chosen distance to the center of the calculated spark (to simulate possible out-of-focus recording).

Generation of artificial model sparks

Artificial "model sparks" with known underlying release waveform were generated using two-photon excited-flash photolysis (TPEFP) of the Ca^{2+} cage DM-Nitrophen (Kaplan and Ellis-Davies, 1988). Solutions for flash photolysis were prepared in a basic solution containing 140 mM KCl and 20 mM HEPES, pH 7.4. To this solution 0.8 mM DM-Nitrophen (Calbiochem, Alexandria, Australia) and 100 μM Fluo-3 (Molecular Probes, Eugene, OR) were added. $CaCl_2$ was added to this solution to set the free Ca^{2+} concentration to 100 nM. Illumination for two-photon excitation was provided by a modelocked Ti:Sapphire (Ti:S) laser tuned to a wavelength of 730 nm. After passing through a Pockels cell (Conoptics, Danbury, CT) the light was coupled into a modified confocal microscope (Zeiss LSM 410, Jena, Germany) and focused to a stationary spot parfocal with the confocal image plane. The PSF of photorelease was determined by uncaging immobilized caged fluorescein-dextran (0.5 μm in plane and 1.4 μm axially; Soeller and Cannell, 1999b). The distance between the focus and the cover slip was ~20 μm to avoid edge effects. Fluorescence changes during the spot photolysis were monitored using the 488-nm line of an argon ion laser (Uniphase, San Jose, CA) in the confocal line-scanning mode of the microscope. The pinhole was set to a diameter of ~1.5 Airey units, resulting in a PSF with an FWHM diameter of 400 nm in plane and 900 nm in the axial direction. Accurate axial alignment between the photolysis spot (near-infrared light from Ti:S laser) and the recording plane (488 nm light from the Ar^+ laser) was assured by adjustment of a lens in the Ti:S beam path, which corrected longitudinal chromatic aberration (Soeller and Cannell, 1999b). During line-scan imaging, the scan line either passed through the center of the photolysis spot (in-focus recording) or was offset from the center by 600 nm (out-of-focus recording). Flash intensities were kept low (<1 mW at the sample) to prevent photobleaching of fluo-3 and cage depletion at the site of photolysis (confirmed by the square dependence of released Ca^{2+} on flash intensity). The fluo-3 fluorescence excited by the stationary uncaging beam was negligible in comparison to that excited by the 488-nm monitoring beam (<2%). Between 30 and 480 responses were averaged to improve the signal-to-noise ratio of line-scan images of model sparks. Due to the two-photon nature of the excitation process, the photolysis rate is expected to be proportional to the square of the flash intensity. To measure the squared flash time course (for comparison with the reconstructed release time course) we also measured two-photon excited fluorescence in a dilute solution (100 μM) of fluorescein in response to flashes that were used to generate model sparks.

Parameters for flux reconstruction from artificial sparks

Reconstruction of the fluxes underlying artificial sparks generated by two-photon excited-spot photolysis of DM-Nitrophen required estimation of its binding and transport parameters. The diffusion coefficient of DM-Nitrophen (D_{DM}) in water was estimated as $4 \cdot 10^{-6}$ cm^2/s using a similar procedure to that used to estimate D_{F3} above. On and off rates for DM-Nitrophen were $3 \cdot 10^7$ $M^{-1}s^{-1}$ and 0.144 s^{-1}, respectively (Escobar et al., 1997). The on and off rates for Ca^{2+} binding to fluo-3 in the salt solution used were $2 \cdot 10^8$ $M^{-1}s^{-1}$ and 150 s^{-1}, respectively, resulting in a K_d of 0.75 μM (similar to that determined by Escobar et al., 1997). Note that proteins were not present in our flash solutions and D_{F3} was, accordingly, $3 \cdot 10^{-6}$ cm^2/s.

Implementation of flux reconstruction algorithms

The first method of reconstructing the SR Ca^{2+} release flux that was implemented was similar to that used by others (Blatter et al., 1997; Rios et al., 1999). Three different algorithms with two different fluo-3 binding schemes were implemented. Figure 1 shows an overview of the dye reaction models underlying these algorithms. The first algorithm (called the "simple binding algorithm" or SBA) corresponded to a simplified fluo-3 binding scheme that takes fluo-3 binding to immobile structures into account by using a lower apparent diffusion coefficient ($D_{F3,app}$) and changed binding rate constants (to reflect the reduced apparent Ca^{2+} affinity resulting from protein binding in the cytosol). Algorithms of the SBA type have been used in previous studies (Blatter et al., 1997; Luky-

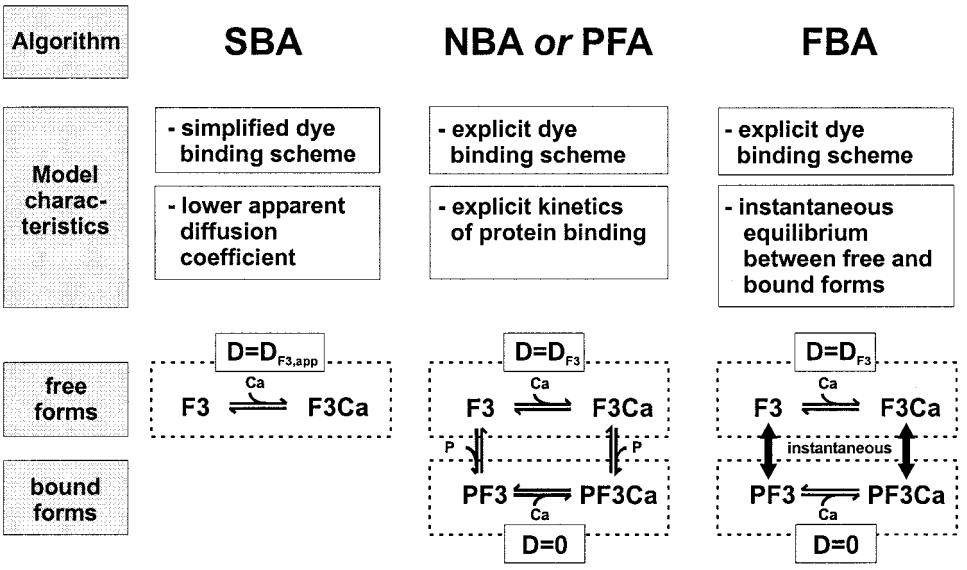

FIGURE 1 Comparison of the algorithms used for flux reconstruction. The dye binding models the algorithms are based upon are shown schematically in this figure. The SBA is based on a simplified binding scheme that takes dye binding into account by using a reduced apparent diffusion coefficient and reduced binding rate constants. The dye binding model underlying the NBA and the PFA explicitly considers both freely diffusing and protein-bound immobile forms of the indicator. Additionally, it takes the nonequilibrium properties of reversible dye binding to proteins into account. The FBA uses an approximation of the dye-binding scheme underlying the NBA. In this scheme, free and protein-bound forms of the indicator are also explicitly accounted for, but the reversible binding of fluo-3 to immobile proteins is always in local equilibrium. F3, freely diffusing Ca-free fluo-3; F3Ca, freely diffusing fluo-3–Ca complex; PF3, protein-bound Ca–free fluo-3; PF3Ca, protein-bound fluo-3–Ca complex; P, immobile protein; D, diffusion coefficient of respective form of indicator; D_{F3}, free diffusion coefficient of fluo-3 in the cytoplasm; $D_{F3,app}$, reduced apparent diffusion coefficient of fluo-3 in the cytoplasm.

anenko et al., 1998; Rios et al., 1999). The second algorithm (called the "nonequilibrium binding algorithm" or NBA) was based on the reaction scheme given by Harkins et al. (1993, see also Fig. 3 *A* and Table 1). The NBA considers separate freely diffusing and protein bound forms of the indicator. Furthermore, the kinetics of reversible protein binding was explicitly modeled. The third algorithm (called the "fast binding algorithm" or FBA) was an approximation to the NBA, which also considered freely diffusing and bound forms of the indicator but additionally assumed that protein binding was instantaneous as described by the respective dissociation constants of the Harkins scheme (cf. Table 1). To test the approximation of instantaneous protein binding used in the derivation of the FBA spark, simulations were run using the nonequilibrium dye binding model (corresponding to the NBA), and the binding ratios of fluo-3 and fluo-3-ca to protein were calculated (i.e., [PF3]/([P][F3]) and [PF3Ca]/([P][F3Ca]), respectively). Using a release current amplitude of 10 pA and starting from a resting $[Ca^{2+}]$ of 100 nM, both ratios remained within $<4\%$ of their equilibrium values. The NBA and FBA were developed as part of this work, and a detailed description is given in the Appendix.

All algorithms involve three main steps. First, an estimate of the distribution of Ca^{2+}-bound fluo-3 was calculated from the normalized fluorescence data (F/F_0). F/F_0 was obtained by dividing the fluorescence transient by the resting fluorescence recorded before the spark. Next, the underlying Ca^{2+} distribution was computed (using Eqs. A9 (SBA) or A13 and A17–A19 when using the NBA and FBA, respectively). Finally, the Ca^{2+} release flux (q_{Ca}) was calculated using both the fluo-3-Ca complex data and the previously calculated Ca^{2+} distribution (according to Eq. A10 for the SBA or Eqs. A7 and A20 for the FBA and NBA). A more detailed description of the procedure is contained in the Appendix.

The calculation of the time course of $[Ca^{2+}]$ and q_{Ca} required numerical derivatives of image data with respect to time and space (cf. e.g., Eqs. A4 and A7). Numerical derivatives were computed using standard finite differencing schemes on a pixel-by-pixel basis when the input data was essentially noise free (e.g., when using simulated data). The pixel spacing in time and space was typically 1 ms by 0.15 μm, and time and space derivatives were estimated using backward and centered differences, respectively. Because numerical differentiation is very sensitive to noise in the input data, filters were used to minimize noise amplification when dealing with noisy experimental (confocal) input data. We used Savitzky-Golay filters, a class of polynomial smoothing filters that have been shown to be useful for smoothing and differentiating noisy experimental data (Bromba and Ziegler, 1981; Ziegler, 1981; Press et al., 1992). These filters are characterized by the order of the smoothing polynomial, and the width N of the filter (which is equal to the number of filter coefficients). For signals that have a Gaussian shape, the optimal width of a Savitzky-Golay filter of order 4 is 1.72 times wider than the FWHM of the signal (Bromba and Ziegler, 1981). With a typical spark width of $\sim$2 μm and a sampling resolution of 0.15 μm, the spark FWHM equals $\sim$13.3 pixels and the optimal N is thus $\sim$23. We chose slightly weaker filtering to preserve more high-frequency content and a filter of order 4 and width 19 was used in experimental reconstructions.

Because the line scan images only contain data along one spatial dimension, an assumption was necessary to allow calculation of the Laplacians in the diffusion/reaction equations. Assuming an approximately spherically symmetric fluorescence distribution, we used the Laplacian in spherical coordinates,

$$\Delta = \frac{\partial^2}{\partial r^2} + \frac{2}{r}\frac{\partial}{\partial r}. \tag{2}$$

The center of the spark was determined by fitting a Gaussian to the spark profile at the peak of the fluorescence transient. The singular behavior of the spherical Laplacian in Eq. 2 close to the center of the spark ($r = 0$) was avoided by using the Cartesian form there:

$$\Delta = 3\,\frac{\partial^2}{\partial r^2}. \tag{3}$$

This approach is different from that used by Blatter et al. (1997), who applied the latter form of the Laplacian everywhere.

Numerical integration of diffusion equations during the reconstruction procedure was performed using FACSIMILE. In some cases, the calculated Ca^{2+} distributions were post-processed by a Gaussian smoothing filter (FWHM 0.25 μm $\times$ 1.5 ms) before the release flux was determined. Buffer species concentrations, binding parameters, and diffusion coefficients used in the calculations were identical to those described under Numerical Modeling. The reduced diffusion coefficient $D_{F3,app}$ for the SBA was obtained from the free diffusion coefficient D_{F3} by reducing it in proportion to the mobile dye fraction (determined at resting [Ca^{2+}] from the Harkins scheme). On and off rates of $0.8 \cdot 10^{-6}$ $M^{-1}s^{-1}$ and 80 s^{-1}, respectively, were used in the SBA reconstruction, similar to values used in previous studies (Blatter et al., 1997; Smith et al., 1998).

The total Ca^{2+} current (I_{spark}) was computed from the reconstructed release flux q_{Ca} by volume integration,

$$I_{spark} = 4\pi \int r^2 q_{Ca}\, dr \approx 4\pi \sum r_i^2 q_{Ca,i} \Delta r, \qquad (4)$$

where r_i and $q_{Ca,i}$ are the radius and release flux at pixel number i, respectively. To partially remove the optical blurring due to the microscope line scan, images were enhanced by digital deconvolution using an iterative maximum-likelihood algorithm (Soeller and Cannell, 1999a) prior to flux reconstruction. The PSF used in the procedure had an FWHM of 0.4 μm, reflecting the experimentally observed in-plane resolution. All data-processing routines were implemented in PDL (http://pdl.perl.org).

Flux reconstruction by parameter fitting

An alternative approach to reconstructing the fluxes underlying Ca^{2+} sparks is to fit a given model to experimental data by adjustment of the parameters that define the model. If the fit of the model converges to the experimental data, then, within the constraints of the model, we obtain an estimate of the release flux. The primary advantage of the parameter fitting algorithm (or PFA) is its decreased sensitivity to noise in the input data (because no explicit numerical derivatives need to be computed). The fitting procedure was initiated by starting a model simulation run with an appropriately chosen initial SR Ca^{2+} release waveform (that reasonably reproduced the experimental spark in terms of amplitude and width). The simulation program compared the fluorescence time course of the computed spark to that of the experimental spark at each point of a regular sampling grid over a period of 35 ms and computed a residual sum of squares of differences. In subsequent runs, the parameters characterizing the release waveform were varied to minimize the residual sum of square differences until the best fit was obtained. This was indicated by a reduction of the residual square error to within a range that was expected based on the noise in the experimental data (using an estimated accuracy of $\sim$5% of the average spark data). The whole fitting process was automated under control of the simulation package FACSIMILE (Chance et al., 1977) that was used to implement our spark model as described in Numerical Modeling above. The release waveform q_{Ca} was defined by seven adjustable parameters I_0, t_1, τ_1, t_2, τ_2, σ_0 and σ_s,

$$q_{Ca}(r, t) = \frac{I_0}{2F(\sqrt{\pi}\sigma)^3}\, e^{-r^2/\sigma^2} f(t), \qquad (5)$$

where F is Faradays constant. The width of the release region σ was a function of the two parameters σ_0 and σ_s and could change linearly in time when $t > t_1$:

$$\sigma = \sigma_0 + \sigma_s(t - t_1). \qquad (6)$$

The temporal shape of the release waveform was a product of two Boltzmann equations:

$$f(t) = \frac{1}{1 + e^{-(t-t_1)/\tau_1}} \frac{1}{1 + e^{(t-t_2)/\tau_2}}. \qquad (7)$$

By appropriate choice of time constants t_1, τ_1, t_2, and τ_2 this function can assume approximately rectangular shapes and exponentially decaying/rising time courses (see Results). The experimental input sparks used as a fitting target were digitally deconvolved prior to fitting (using an iterative maximum-likelihood algorithm as described above) to remove the blurring by the microscope. The dye binding model and parameter set (describing dye binding, Ca^{2+} buffering and diffusion) used in the fitting process were identical to those used with the NBA (see also Fig. 1).

Imaging of rat cardiac myocytes

Enzymatically isolated rat cardiac myocytes were prepared as described elsewhere (Evans and Cannell, 1997) in accordance with the *Guide for the Care and Use of Laboratory Animals* published by the National Institutes of Health (NIH publication No. 85-23 1985). Briefly, 250-g Wistar rats were killed by lethal injection of pentobarbital (100 mg/kg) and hearts quickly mounted on a Langendorff perfusion system. After initial perfusion with a nominally Ca^{2+} free solution (containing in mM: NaCl, 120; KCl, 5.4; HEPES, 10; pyruvate, 5; glucose, 20; taurine, 20; pH 7.05 with NaOH) for 5 min 4 U/ml protease (Sigma type XXIV), 1 mg/ml collagenase (Worthington type II) and 100 μM $CaCl_2$ were added. After 10–12 min of enzyme treatment, the ventricles were cut free and chopped into small pieces. A series of triturations was performed using a wide-bore pipette. The resulting cell suspension was filtered through gauze and diluted with solution containing 100 μM $CaCl_2$. The free Ca^{2+} concentration was gradually increased to 2 mM, and the final cell suspension was stored at room temperature.

For line-scan imaging, cells were incubated with 5 μM of the AM form of fluo-4 for 25 min at room temperature (20–22°C). The cells were then placed in the basic solution with 2 mM $CaCl_2$ and 10–20 μM of nifedipine. (The nifedipine concentration was adjusted to allow identification of well-separated spark sites.) The labeled cells in the nifedipine solution were placed in the chamber of a confocal microscope (Zeiss LSM 410) that had a glass coverslip as its bottom. To image repeatedly active spark sites, a protocol similar to that used by Bridge et al. (1999) was used. Trains of action potentials were invoked by field stimulation at a frequency of 0.33 Hz. Indicator fluorescence was excited using the 488-nm line of an argon laser and detected between 510 and 550 nm (HQ filter, Chroma Technology, Brattleboro, VT). Fifty confocal lines were acquired during each field stimulation. The field stimulus was triggered after the first 10 lines and the resulting Ca^{2+} transients were recorded during the remaining 40 line scans. Line scanning was performed at the maximum scan speed of 1.4 ms/line. The total exposure time was therefore 70 ms/stimulus, and trains of up to 100 stimuli could be recorded without detectable cell damage. Images were stored to hard disk for off-line analysis.

Data analysis

Line-scan images were analyzed using custom routines written in IDL (Research Systems Inc, Boulder, CO). The fluorescence during the prestimulus period was averaged and used to calculate self-ratio images by dividing the recorded fluorescence transient by the resting fluorescence intensity. To compute average sparks, all line scan images of a stimulation series were displayed and those spark sites manually selected that gave rise to sparks that were well separated from neighboring sites (to avoid contributions from Ca^{2+} release originating at adjacent sites). After analyzing 30 individual experiments, three spark sites were found that would be suitable for full analysis. Although the stimulus occurred at a fixed time

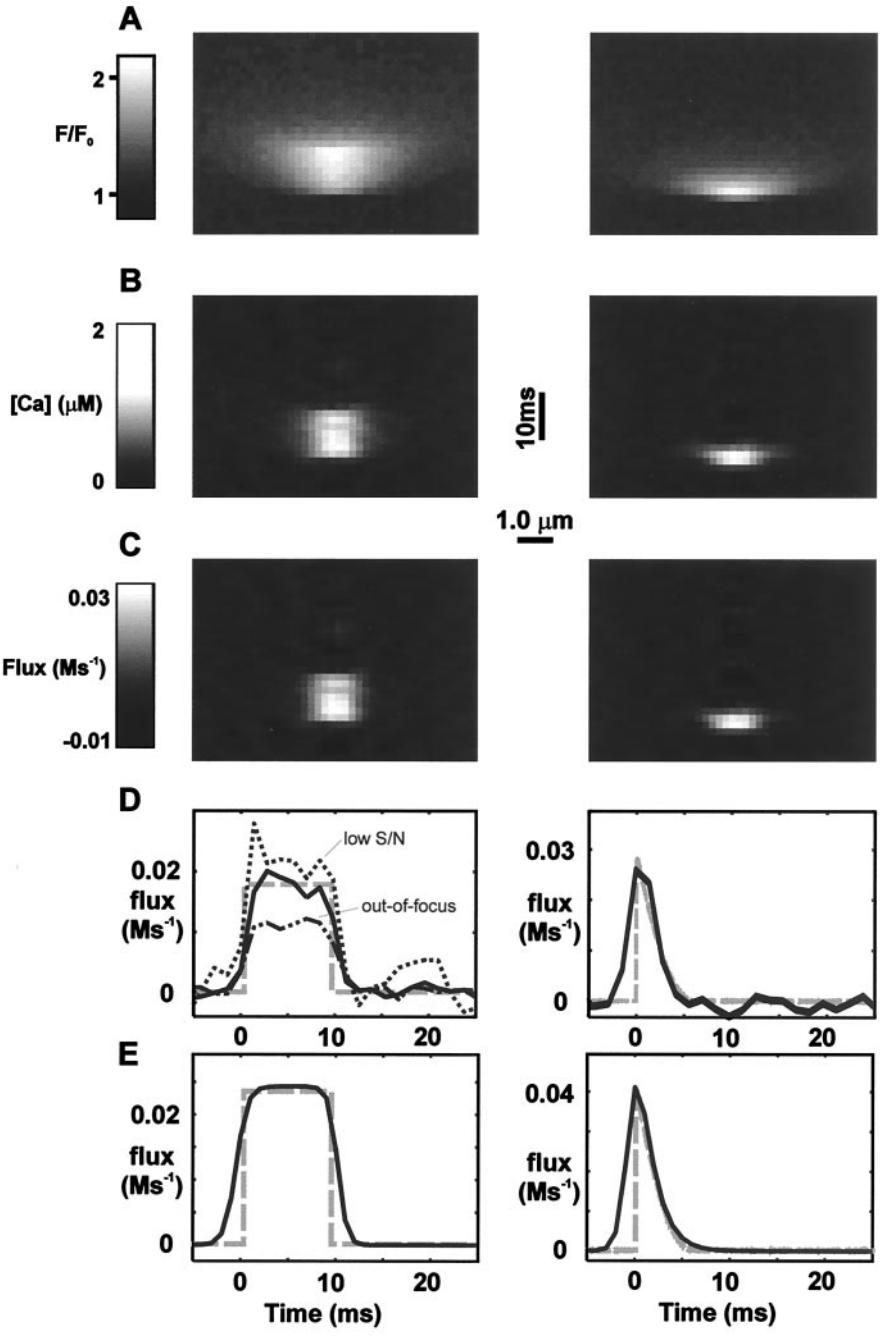

FIGURE 2 Experimental tests of Ca^{2+} release flux reconstruction. Artificial model sparks were generated by two-photon spot photolysis of the Ca^{2+} cage DM-Nitrophen with brief flashes of light from a Ti:Sapphire laser. Ca^{2+} release was monitored by imaging the fluorescence changes of the indicator fluo-3 in confocal mode. (*A*) Two line-scan images of normalized fluorescence (F/F_0) recorded in response to an uncaging flash with a step time course (*left*) and a flash with an exponentially decaying time course (*right*). (*B*) The Ca^{2+} distributions that were reconstructed. (*C*) The resulting flux estimates. A comparison of the reconstructed flux time courses (*solid lines*) with the squared time course of the flash intensities (*dashed lines*—measured by two-photon fluorescence of fluorescein) shows good agreement (*D*). (*D*) The left panel also shows release time courses (*dotted*) reconstructed from fluorescence data that was recorded out of focus (600 nm) or had an ~4 times lower signal-to-noise ratio (*dashed*). (*E*) Release time courses reconstructed with the PFA. In all line-scan images, time increases from the bottom to the top. This convention was also adopted in the remaining figures.

with respect to the start of the scan, sparks were activated with a jitter of 1–2 lines (that was presumably due to the latency of L-type channel opening). This jitter was removed by aligning the rising phase of sparks before averaging.

RESULTS

Flux reconstruction from model sparks

To critically test the ability of our flux reconstruction method to reconstruct the local release flux, we estimated the flux underlying artificial model sparks produced by TPEFP. Example line-scan images of model sparks generated by TPEFP in the DM-Nitrophen solution are shown in Fig. 2 *A*. The left-hand panel shows images recorded in response to a Ca^{2+} step release generated by switching the photolysis spot on for 10 ms. The right-hand panel shows responses to an illumination time course that resulted in a release spike, which decayed approximately exponentially with a time constant of 4 ms. Using the SBA (because no immobile buffers were present in the test solution) the underlying [Ca^{2+}] distributions and Ca^{2+} release fluxes were calculated, and Fig. 2 *B* shows that the [Ca^{2+}] reaches a concentration of ~1 μM in the center of the photolysis spot, similar to the [Ca^{2+}] concentrations achieved during a

cardiac Ca^{2+} spark. The reconstructed Ca^{2+} flux peak amplitudes were ~30 mM/s (Fig. 2 *C*). The time course of photolysis was measured by applying the same illumination waveforms to a solution of fluorescein and recording the resulting fluorescence time course (see Methods). Comparison of the reconstructed release time course with that measured by fluorescein shows good agreement in both cases (Fig. 2 *D*). Similarly, the release time course reconstructed with a variant of the PFA (that used a SBA-type dye-binding model) agrees well with the expected time course (Fig. 2 *E*). The fluxes calculated with the PFA were slightly larger than those calculated with the SBA. This was largely explained by the fact that the release region reconstructed with the PFA was slightly narrower (data not shown).

These results show that our reconstruction methods can distinguish between the square step and a spiked release waveform. In the case of the step-shaped release waveform, the effects of a lower signal-to-noise ratio (decreased by a factor of ~4) and out-of-focus recording were also tested (Fig. 2 *D*). Although the reconstructed release waveform was clearly more noisy when using the lower signal-to-noise input data, the general square step shape was still reproduced. Using slightly out-of-focus (600 nm) input data, the waveform was similar to that of the in-focus reconstruction but reduced in amplitude.

Numerical tests of flux reconstruction algorithms

A number of numerical tests of the performance of the flux reconstruction algorithms were carried out. It is known that dye binding to proteins occurs in muscle cells (Harkins et al., 1993) and that it must occur reversibly with finite on and off rates (for thermodynamic reasons). Therefore, the reversible dye binding model underlying the NBA was used to generate the simulated sparks because it reflects these dye properties most accurately (among the models used in this study, cf. Fig. 1). Simulated fluorescence records were calculated using a square step-release waveform corresponding to a release current of 11 pA. For ideal conditions, the fluorescence records were not blurred and represented an in-focus recording through the center of the spark site. The results generated by the NBA were, as expected, in good agreement with the simulated $[Ca^{2+}]$ release fluxes, as shown in Fig. 3 *B*. The FBA (that used only the experimentally observable concentration of TF3Ca) also produced reasonable time courses but with slightly increased amplitudes (Fig. 3 *C*). In contrast, estimates produced by the SBA showed large discrepancies with regard to time course, spatial distribution and amplitude of both $[Ca^{2+}]$ (not shown) and q_{Ca} (Fig. 3 *D*). These major errors occurred despite the fact that the effective diffusion coefficient for fluo-3 in the reconstruction was reduced in direct proportion to the level of dye binding to proteins (i.e., D_{F3} was reduced by a factor of 0.13 because 87% of the dye was bound to protein). Because all previous studies have used a modification of the diffusion coefficient (to mimic the effects of dye binding) we suggest that, in general, the release flux will have been underestimated. To mimic the PSF of our confocal microscope the simulated fluorescence transient was blurred using a Gaussian-shaped kernel (FWHM $0.4 \times 0.4 \times 0.9$ μm in *x*, *y*, and *z*, respectively). In the presence of optical blurring and recording from a line that passed through the center of the spark (in-focus recording, Fig. 3 *E*), the fast-binding algorithm produced a release flux estimate that was spatially wider than the underlying release region (~0.7 μm versus 0.4 μm). As might be expected, the calculated peak flux amplitude was reduced (~8% of the correct amplitude when using the FBA). However, the integral of the flux was only slightly reduced when compared to the actual amplitude (~8 pA versus 11 pA). The effects of blurring could be partly restored by deconvolving the line-scan data prior to reconstruction. Using the deconvolved data, the amplitude was restored to ~20% of the correct one and the integrated current was nearly fully recovered (~10 pA). The reconstructions generated by the SBA underestimated peak flux and integrated flux more severely. When the input data was further degraded by recording out-of-focus (600 nm from the center of the spark site, Fig. 3 *F*) a further reduction in flux was observed (~4 pA versus 11 pA for the FBA), which was only partially recovered by deconvolution.

When model sparks with exponentially decaying release time courses were modeled, the FBA reported that the release time course was sensitive to the amplitude of the release function (Fig. 4 *A*). In Fig. 4 *B*, this artifact of the FBA is examined for release fluxes between 0.5 and 16.5 pA. Over this range, the calculated release time constant varied between ~120% and ~80% of the actual release function time constant (7 ms). When the SBA was applied to the same data, the distortion of the calculated release time course was more severe (compare Fig. 4 *A* and *C* with *B* and *D*). For the smallest release flux (0.5 pA), the error was small (~2%) whereas, for the largest release flux (16.5 pA), the error increased so that the reconstructed time constant was only 37% of the actual time constant (Fig. 4 *D*). These results suggest that caution must be applied to the interpretation of release waveforms calculated from Ca^{2+} sparks of different amplitudes, a problem compounded by the use of the SBA. In connection with this point, it has been suggested that large amplitude sparks are associated with a faster decaying release flux (Lukyanenko et al., 1998).

To test for linearity in the relationship between the reconstructed release current amplitude and the actual current amplitude, release currents were calculated from simulated Ca^{2+} sparks with different release flux amplitudes. Blurring and a defocus of 600 nm was applied to the simulation data. The results are summarized in Fig. 5 *A*, which shows that the amplitude of the reconstructed release current is essentially proportional to the actual release current. However,

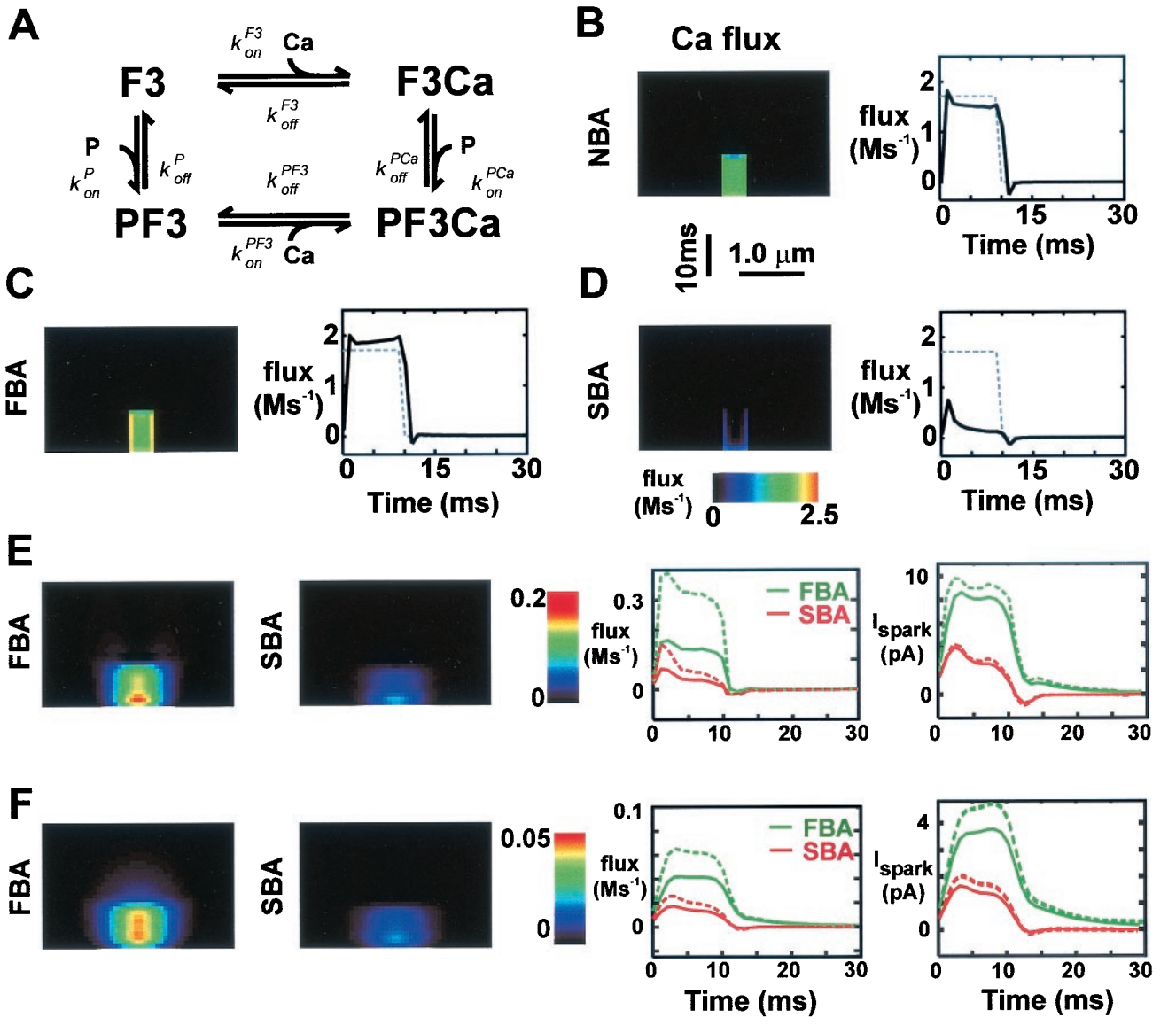

FIGURE 3 Numerical tests of flux reconstruction algorithms. (*A*) The Harkins scheme of fluo-3 binding that was used in numerical calculations to generate simulated spark records. F3, freely diffusing fluo-3; F3Ca, freely diffusing fluo-3–Ca complex; PF3, protein bound fluo-3; PF3Ca, protein bound fluo-3–Ca complex. The values of the various binding constants are listed in Table 1. (*B–D*) Ca^{2+} and Ca^{2+} release flux distributions reconstructed from a simulated spark record with an underlying square release waveform that had an amplitude of 11 pA. The simulated spark data was not blurred and the recording line was placed through the center of the spark. The graphs show the reconstructed Ca^{2+} release flux time course at the center of the spark (*solid lines*) compared to the actual time course extracted from the model (*dashed*). The reconstructions in (*B*), (*C*), and (*D*) were calculated with the NBA, FBA, and SBA, respectively. (*E*) Reconstructions of Ca^{2+} release flux calculated with the FBA and the SBA using blurred input data. The graphs of release flux and integrated current (I_{spark}) show that blurring results in an underestimation of the "true" quantities. This effect is increased when recording from an out-of-focus location (600 nm from the center of the spark site, *Panel F*). The graphs show the results of reconstructing from the raw (*solid lines*) and deconvolved data (*dashed lines*).

the reconstructed release amplitudes systematically underestimate the true current by a factor of ~2.5 (without deconvolution) or ~2.2 (with deconvolution). This effect was due to the out-of-focus recording (see also Fig. 3 *F*). The effect of defocus is explored in Fig. 5 *B*. For no defocus, the FBA reports a peak release flux of 77% of the actual, and this figure decreased with increasing defocus to 15% at 1 μm when the raw blurred data was used as input. With deconvolution prior to reconstruction the peak release flux is restored to ~95% for an in-focus spark and decreases to ~16% at 1 μm.

The novel PFA was also tested in a numerical experiment. To demonstrate that the PFA can distinguish between abruptly terminating and more gradually decaying release waveforms, it was used to reconstruct the fluxes underlying two noisy simulated sparks. To simulate the photon noise in

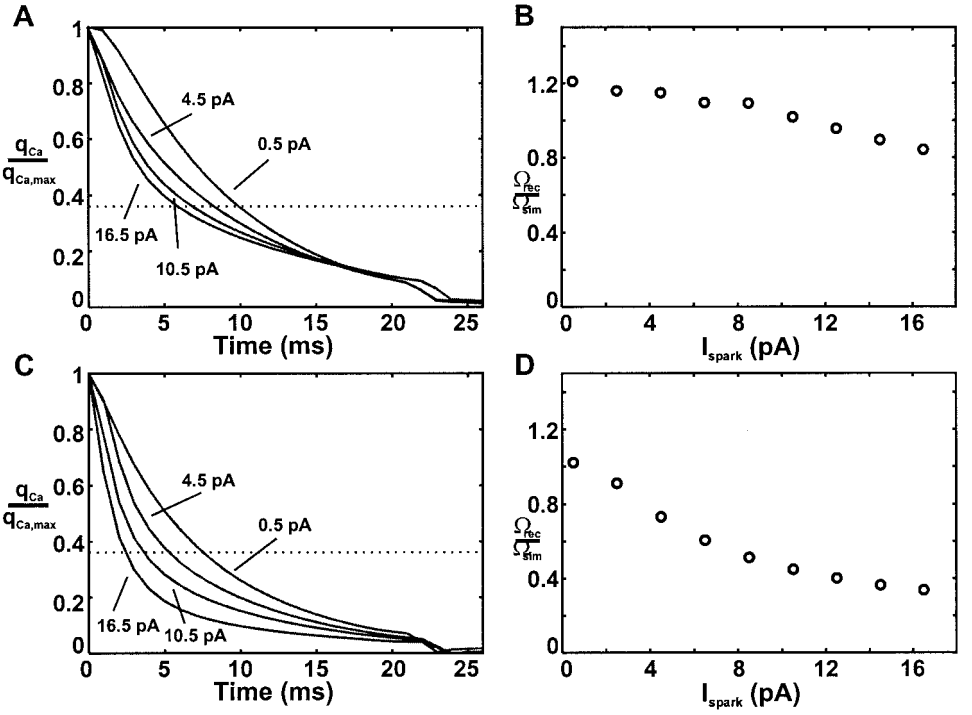

FIGURE 4 Amplitude dependence of reconstructed release flux time course. The FBA and SBA were used to reconstruct the Ca^{2+} release fluxes underlying simulated sparks that had an exponentially decaying time course (time constant (τ_{sim}) 7 ms) and varying release current amplitude. (*A*) Time courses of Ca^{2+} release fluxes reconstructed with the FBA for simulated release current amplitudes (I_{spark}) of 0.5, 4.5, 10.5, and 16.5 pA. (*B*) The reconstructed time constants (τ_{rec}) obtained from fits to reconstructed release flux traces for current magnitudes varying between 0.5 and 16.5 pA. (*C*) and (*D*) Corresponding graphs of reconstructions that were calculated with the SBA.

experimental spark records, Poisson noise corresponding to a signal of 150 photon counts at the peak of the fluorescent transient was added to the simulated spark data. Figure 6, *A* and *B*, show results of using the PFA to reconstruct the release flux underlying a spark that resulted from a fast rising and exponentially decaying release waveform. The reconstructed release flux (that resulted in the best fit to the noisy data) approximated the actual waveform well (Fig. 6 *B*). Note that the release flux reconstructed from the same data using the FBA was more noisy. A second simulated spark that was generated using a nearly rectangular-shaped release waveform was also well fit with the PFA (Fig. 6 *C*). Figure 6 *D* shows that the reconstructed release flux reproduced the abrupt onset and termination of release (albeit with slightly increased rise and fall times). Notably, the reconstructed fluxes calculated with the PFA were largely unaffected by the noise in the simulated spark records.

These results suggest that the FBA and the PFA (but not the SBA) can provide a good estimation of actual release currents. As noted above, a problem in reconstructing the fluxes underlying Ca^{2+} sparks is the generally poor signal-to-noise ratio associated with their recording. Reconstruction tests using records of individual sparks suggested that the reconstruction algorithms are so sensitive to noise as to render the reconstructed flux distribution almost useless (data not shown). This was the case for previously published (SBA) and algorithms developed in this study (NBA, FBA, PFA). To ameliorate this problem, we can apply signal averaging to Ca^{2+} sparks recorded from well-separated, individual Ca^{2+} spark sites (Bridge et al., 1999). This pro-

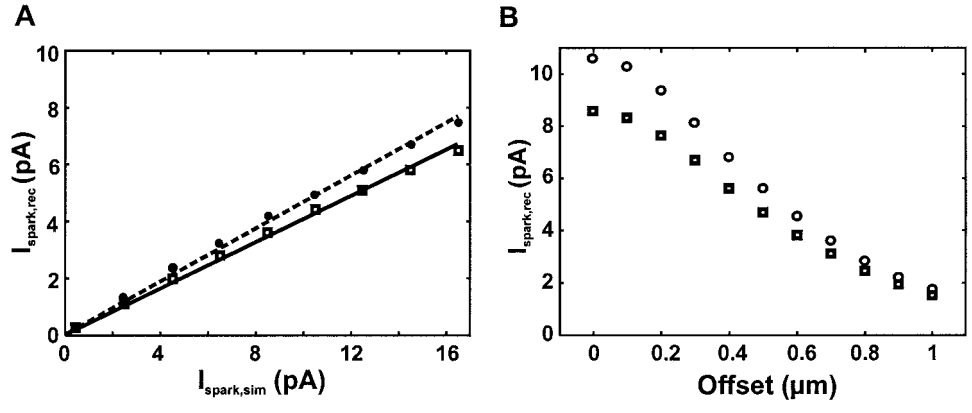

FIGURE 5 Summary graphs of algorithm performance. The reconstructions were performed with the FBA. (*A*) The relationship between the magnitude of the release current in the simulation ($I_{spark,sim}$) and the reconstructed release current ($I_{spark,rec}$) suggesting that the relationship is linear. (*B*) A graph of the dependence of the reconstructed release current on the degree of defocus for a fixed simulation current of 11 pA. *Circles*, deconvolved input data; *squares*, raw input data.

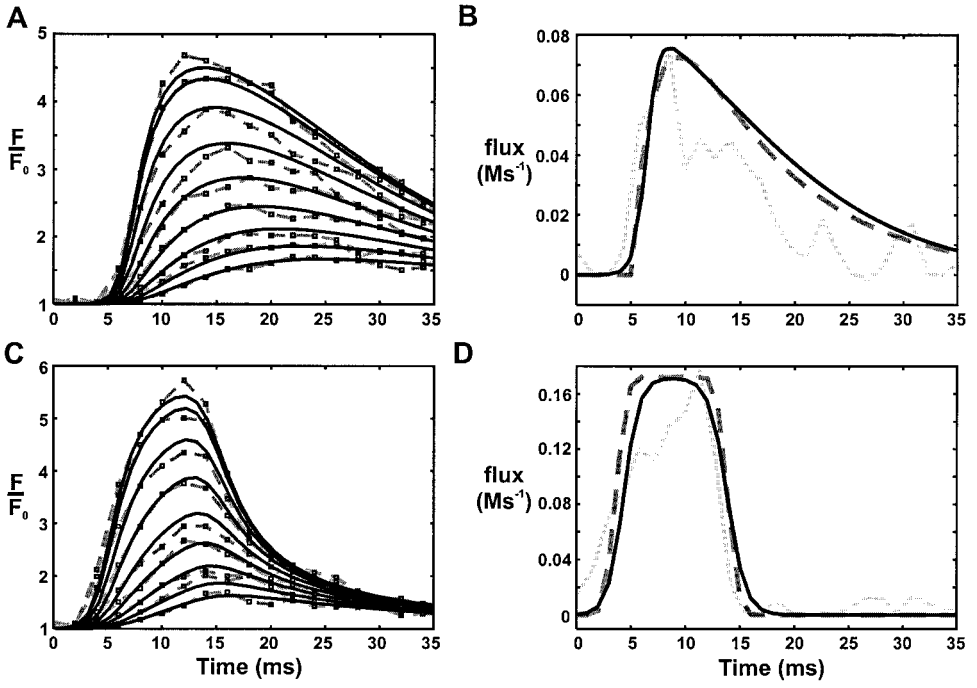

FIGURE 6 Reconstruction of SR Ca^{2+} release flux by parameter fitting. The PFA was used to reconstruct the Ca^{2+} release flux underlying two simulated spark records. Poisson noise corresponding to 150 photons at the peak of the fluorescence transient was added to the simulated records. (*A*) and (*B*) The simulated spark used as fitting target was generated with a release function that had an exponentially decaying release time course. (*A*) The fluorescence time course of the best fit spark (*solid lines*) overlaid on data points extracted from the simulated noisy input spark that were used as a fitting target (connected by *dashed lines*). (*B*) The release flux at the center of the simulated spark record is shown (*dashed*) overlaid by the reconstructed release flux waveform that resulted in the best fit of the fluorescence data (*solid line*). (*C*) and (*D*) Corresponding plots of the fitted time course and best-fit release flux using a simulated spark record generated with an approximately rectangular release flux waveform. (*B*) and (*D*) The release flux reconstructed with the FBA is also plotted for comparison (*grey solid lines*).

tocol allows reconstructing the average release waveform at a fixed spark site at steady state. Although it has been suggested that individual Ca^{2+} spark sites respond in a stereotypical way (Bridge et al., 1999), it is possible the release flux time course could vary between individual Ca^{2+} sparks. Although Fig. 5 *A* suggests that the FBA reconstructed flux amplitude scales in proportion to the underlying flux, we also tested whether the release flux computed from the averaged Ca^{2+} spark was the same as the average of fluxes from the individual Ca^{2+} sparks. Figure 7 *A* shows ten simulated sparks where the release waveform deviated randomly from a mean waveform. The time of the upstroke of the underlying step release was exponentially distributed with a mean of 1.5 ms, and the duration of the release step varied exponentially with a mean of 3 ms. Additionally, the amplitude of the release current during the plateau deviated from a mean of 11 pA according to Poisson statistics with a standard deviation of 1.1 pA. The individual release time courses and the average release waveform are shown in Fig. 7 *B*. The Ca^{2+} distribution (Fig. 7 *C*) and release flux (Fig. 7, *D* and *E*) reconstructed from the average spark agree very closely with the averaged Ca^{2+} distribution and the averaged release flux, respectively. This suggests that the flux reconstruction procedures behave approximately linearly and the release flux reconstructed from average sparks at a fixed site will correspond to the average release flux at that site.

Experimental average sparks at fixed sites and flux reconstruction

The above tests suggest that the FBA and the PFA can provide an estimate of the release waveform associated with Ca^{2+} sparks, and that averaging to improve signal-to-noise does not seriously distort the average release flux. Figure 8 *A* shows ten line-scan images (from a sequence of 100) and evoked Ca^{2+} sparks in response to the electrical stimulation are clearly visible. Several repeatedly firing sites can be seen, and individual line-scan images from the sequence were selected on the basis that no adjacent sites appeared to be active (Fig. 8 *B*). Note the stereotypical appearance of these sparks with regard to amplitude and spatial extent in these images, supporting the idea (Bridge et al., 1999) that individual spark sites appear to respond in an all-or-none fashion. Figure 8 *C* shows the spatio-temporal properties of the resulting Ca^{2+} spark obtained by averaging the individual Ca^{2+} spark records. The averaged Ca^{2+} spark was

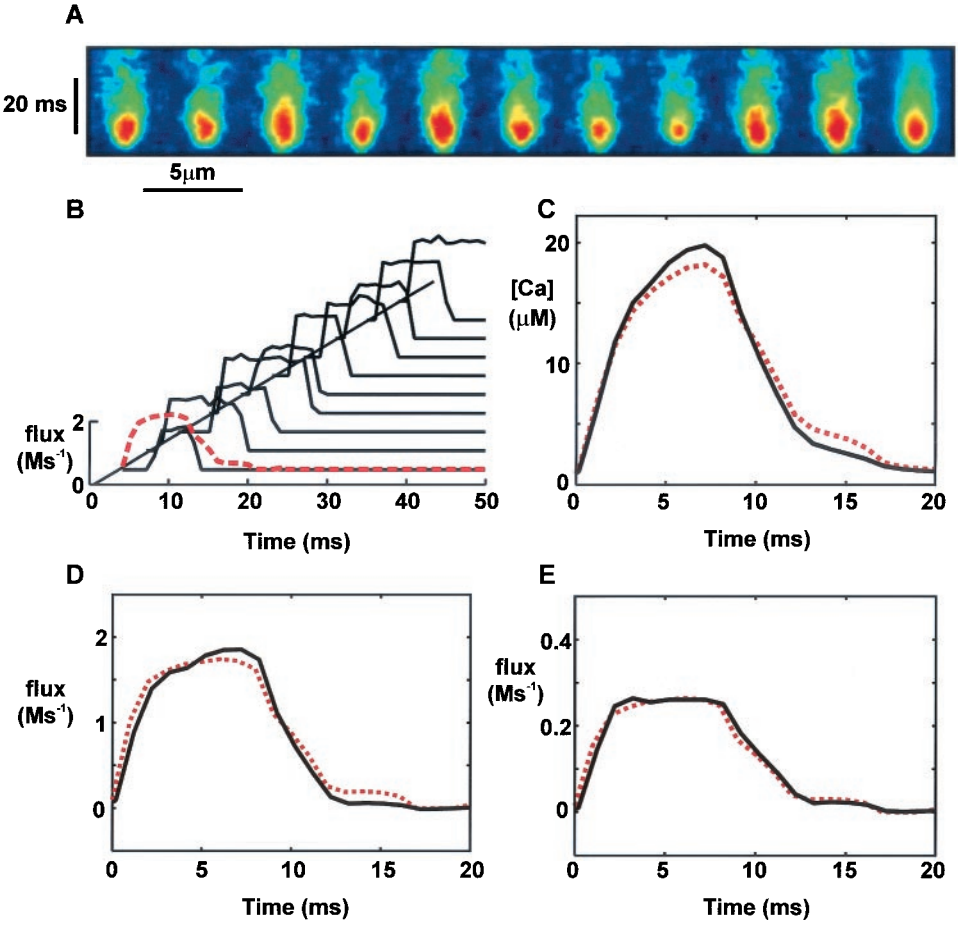

FIGURE 7 Linearity of flux reconstruction. (*A*) The row of images at the top shows ten simulated spark records where the release wave form deviated randomly from a mean release waveform and the resulting average spark. (*B*) The time courses of the release waveforms underlying the simulation of individual sparks and the mean waveform (*red*). (*C*)–(*E*) Compare the time courses of the average Ca^{2+} distribution and the average Ca^{2+} release flux (*red*) to the average of the reconstructed Ca^{2+} and Ca^{2+} release flux time courses. (*D*) The release flux was reconstructed from unblurred in-focus data. (*E*) Optical blurring and a defocus of 600 nm were also included, and the amplitude of the average release flux (*red*) was rescaled to match the reduced average reconstructed release flux when blurring and out-of-focus recording were included.

associated with a peak fluorescence ratio of 3.5 and a spatial extent of ~1.7 μm (FWHM) at the peak. These properties are within the range reported elsewhere (Cheng et al., 1996a; Song et al., 1997).

Figure 9 shows flux reconstructions from three individual Ca^{2+} spark sites. The upper panel shows the averaged Ca^{2+} sparks (Fig. 9 *A*), and the calculated release wave forms using the FBA are shown below (Fig. 9 *B*). Despite averaging, noise in the reconstruction is large, and, without averaging, the computed waveform would probably be useless. Because the deconvolution increased noise in the reconstructed release waveform (data not shown), the FBA calculations were performed on the raw data. Figure 9, *C* and *D*, shows the deconvolved average sparks and the best-fit sparks determined with the PFA, respectively. The release currents (integrated within a radius of 0.7 μm) that were calculated with the FBA and the PFA are compared in Fig. 9 *E*, and peak amplitudes ranged from 7 to 12 pA. The time courses calculated with the FBA and the PFA are in reasonable agreement with respect to rise time and peak amplitude, although the traces calculated with the FBA are generally more noisy. The release currents calculated with the PFA decay approximately exponentially. This point is explored further in Fig. 10, which shows PFA reconstructions of the release flux at the center of the three averaged sparks. Although the amplitudes of these sparks were variable, the time constants of decay of the release flux were all within the range ~7–8 ms.

Because the calculated Ca^{2+} release flux also depends on the values of the various parameters (describing binding and movement of the various species), we performed a sensitivity analysis. The release flux from one of the sparks shown in Fig. 9 was reconstructed using a number of parameter sets in which individual parameters deviated by a factor of 1.5 from our standard parameter set (see Methods). The resulting time courses of Ca^{2+} release flux and integrated current were generally unaffected, but the calculated current amplitudes varied depending on the parameter set. When the fluo-3 affinity was reduced by 50%, the calculated current was increased to 17.2 pA or ~160% of the value calculated with the standard parameter set. A 50% increase in fluo-3 Ca^{2+} affinity resulted in a reduction of the estimated amplitude to ~70%. Changes in the resting Ca^{2+} concentration caused similar changes in the estimated current amplitude (to 170 and 62% when the concentration was increased or reduced by 50%, respectively). We additionally tested the effect of similar changes in D_{F3}, D_{Ca}, total troponin and fluo-3 concentration, and kinetics of fluo-3 bind-

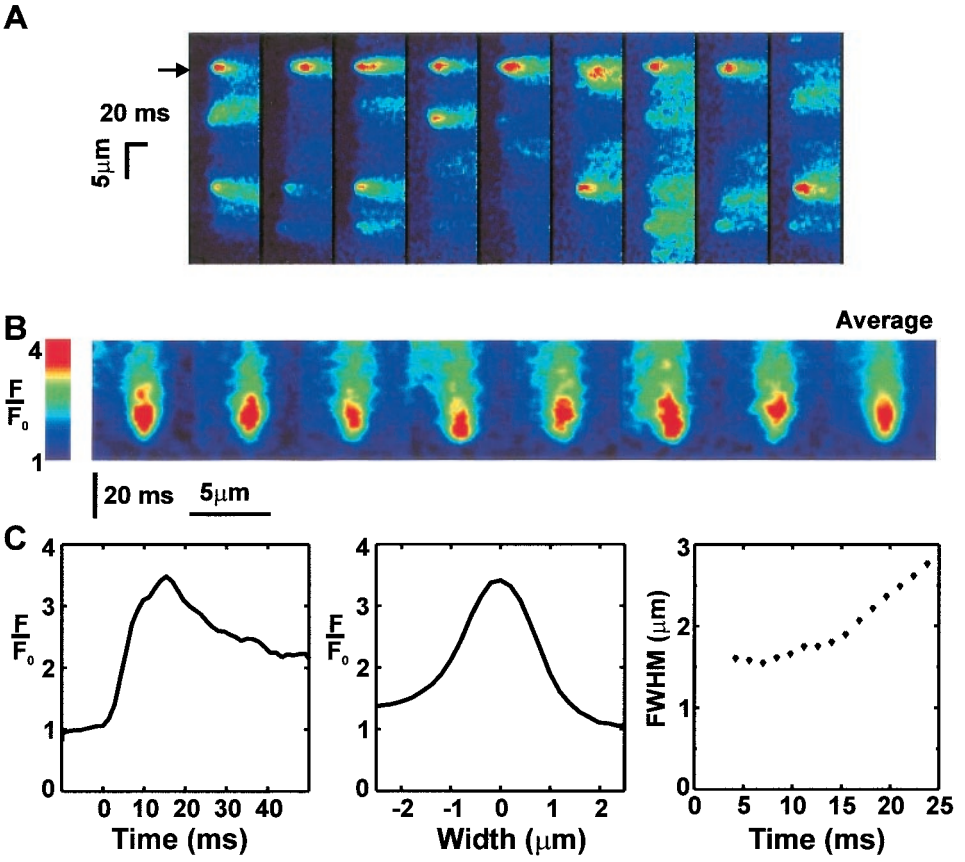

FIGURE 8 Example of sparks recorded in the presence of nifedipine. (*A*) Nine from a sequence of 100 line-scan images recorded in a field stimulated rat cardiac myocyte. A frequently firing site is indicated (*arrow*). (*B*) Several individual sparks from that site and the resulting average spark. (*C*) Graphs showing the fluorescence time course at the center, the spatial fluorescence profile at the peak, and the time course of increase in spark width, summarizing the spatio-temporal characteristics of the average spark.

ing. The resulting changes in current amplitude were less than 20%.

DISCUSSION

In this study, we have tested the ability of four flux reconstruction algorithms to reconstruct local Ca^{2+} fluxes from confocal line-scan images and identified two algorithms that can provide useful measurements of the Ca^{2+} release fluxes underlying Ca^{2+} sparks in rat cardiac myocytes. By using artificial sparks, we provide evidence that our flux reconstruction algorithms produce reliable estimates of the underlying Ca^{2+} fluxes. We have also shown that detailed modeling of dye binding to immobile structures is required for accurate reconstruction, in accord with the conclusions of Hollingworth et al., (2000). Failure to account for dye movement can lead to serious artifacts in flux reconstruction, the most serious of which is a strongly amplitude-dependent time course. Because such a phenomenon has been reported, we suggest that such data need to be re-evaluated using our FBA or PFA. Using these reconstruction algorithms, we have estimated that the release fluxes underlying Ca^{2+} average sparks in rat cardiac myocytes are 7–12 pA in amplitude and last ~10 ms.

Experimental tests of the flux reconstruction algorithm

Although flux reconstruction algorithms have been derived from theoretical models of spark formation (Blatter et al., 1997), the present study provides the first direct test of such methods in an experimental model. To generate artificial Ca^{2+} sparks with known release waveforms, we used the unique ability of two-photon excited flash photolysis to create a local source of Ca^{2+} by photolysis of DM-Nitrophen. Although the region of photorelease was not spherical (but rather the ellipsoidal shape of the microscope PSF) the resulting fluorescence distribution should rapidly become spherical as diffusion takes place. The Ca^{2+} release time course underlying these artificial sparks is known because the rate of photolysis is proportional to the time course of the squared flash intensity (provided the intensity is well below saturating levels, as was the case here—data not shown). It was therefore possible to directly compare the

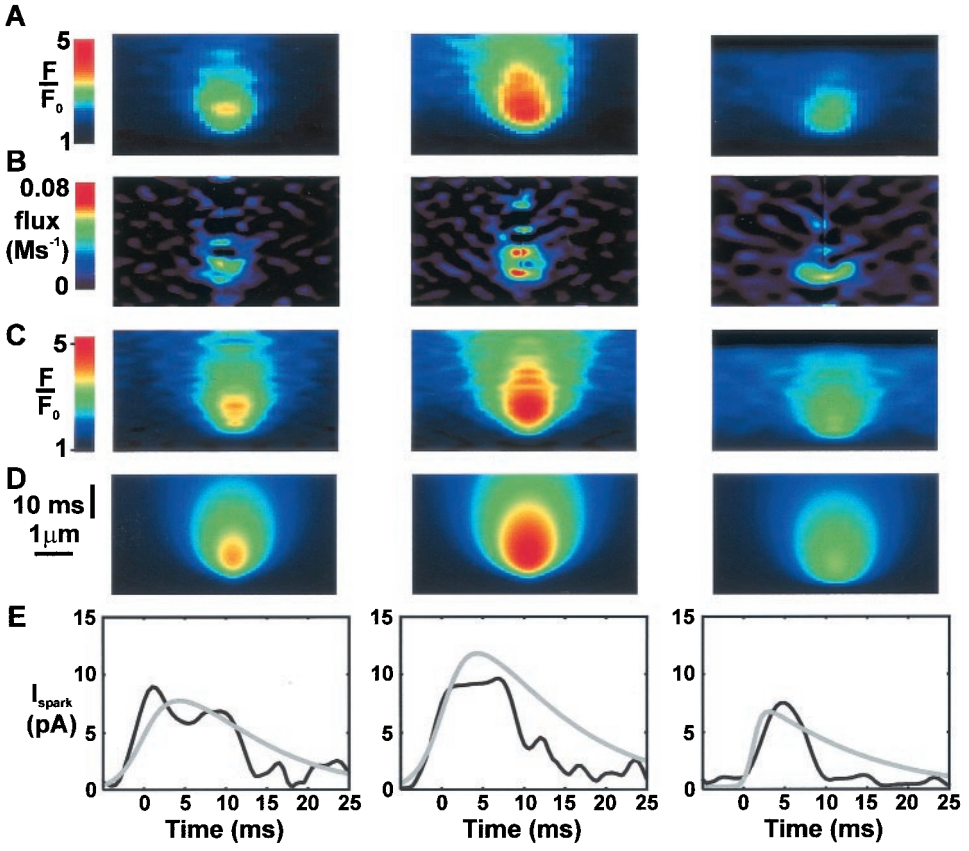

FIGURE 9 Reconstruction of the Ca^{2+} release flux underlying average sparks. (*A*) Averaged sparks from three different sites. (*B*) The corresponding Ca^{2+} release flux distributions calculated with the FBA. (*C*) The deconvolved average sparks are shown above (*D*) corresponding fitted sparks generated with the PFA. (*E*) The integrated release currents calculated using the FBA (*black*) and the PFA (*grey*).

calculated release waveforms to the known release waveform to test the reliability of the algorithms. To our knowledge, this is the first time that any such test of flux reconstruction algorithms has been performed.

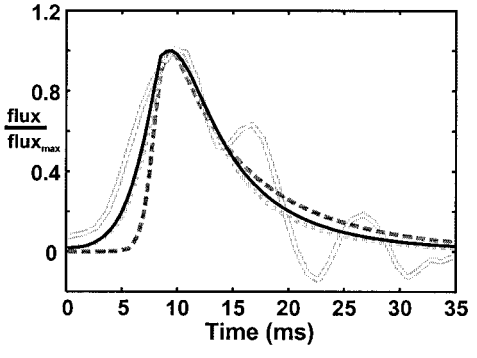

FIGURE 10 Comparison of the reconstructed Ca^{2+} release flux waveforms. An overlay of the release fluxes (calculated with the PFA) at the center of the three average sparks plotted in Fig. 9 shows that the decay times fall within a narrow range of 7–8 ms. Also shown is the normalized reconstructed release time course computed with the FBA from one of the sparks (noisy light gray curve).

To make our tests realistic, we produced artificial sparks, which resembled experimentally recorded Ca^{2+} sparks in terms of size, duration, fluorescence amplitude, and signal-to-noise ratio. The latter factor is particularly important because all inverse reconstruction algorithms (i.e., those that use differentiation) are extremely sensitive to noise. In fact, even with signal averaging, the resulting computed spark release waveform was quite noisy, and, without averaging, would have been useless. Although the PFA is less noise sensitive than other inverse reconstruction algorithms, signal averaging is still important to constrain the fitted release flux distribution. An additional complicating factor resides in the problem that the exact locus of the origin of the spark is unknown. It was therefore of interest to examine the sensitivity of the reconstructed waveform to small amounts of microscope defocus (Izu et al., 1998). We found that, as defocus increased, the reconstructed flux decreased in amplitude with minimal changes of the time course (Fig. 2). It follows that our reconstructions of evoked Ca^{2+} sparks must be a lower limit of the actual release flux, although the release waveforms should be reasonably accurate.

Reversible dye binding and flux reconstruction

Experimental observations suggest that a significant proportion of fluo-3 (>80%) is bound to immobile structures in the cytoplasm (Harkins et al., 1993). In models of Ca^{2+} spark formation, the effect of dye binding is generally approximated by reducing the effective fluo-3 diffusion coefficient in proportion to the estimated bound fluo-3 ratio (e.g., Pratusevich and Balke, 1996; Smith et al., 1998). Such an approach is justified if the binding kinetics are instantaneous and there are no differences in affinity between bound and free forms, and previous studies have used this simplifying approximation (Blatter et al., 1997; Lukyanenko et al., 1998; Rios et al., 1999). We found that a simplified dye binding model (SBA) does not correctly reconstruct the release time course, although optical blurring by the microscope helped reduce the reconstruction error of the SBA (albeit at the expense of a reduced reconstructed flux amplitude, Fig. 3). Prompted by the generally poor performance of the SBA, we developed novel algorithms (the FBA and the PFA) that are based on improved approximations to the Harkins (1993) scheme. The idea that SBA models are inadequate is supported by the observation of intrasarcomeric Ca^{2+} movements in skeletal muscle, which require a more detailed model of dye binding to explain them (Hollingworth et al., 2000). Even in the presence of optical blurring and out-of-focus recording, the FBA reconstructed time course matched the actual time course reasonably accurately, although the peak amplitude was reduced by de-focus and blurring.

Dye binding schemes

We examined three different approaches to account for dye binding. The simplest class of model (SBA) assumes that dye binding can be modeled by a reduction in dye diffusion coefficient. As described above, such models do not adequately describe either the time course or amplitude of the release flux. Even more serious is the fact that the models produce a release flux time course that is strongly amplitude dependent. Clearly, such an artifact would be unacceptable for classes of experiment which seek to relate the time course of RyR inactivation to the amplitude of the Ca^{2+} release flux (Lukyanenko et al., 1998). The next class of model would explicitly deal with protein-bound and free forms of the dye and assume instantaneous equilibration between bound and free forms. We examined this FBA model and showed that it was able to reproduce known release waveforms with a reasonable degree of accuracy. A more complete model also includes the kinetics of the dye–protein interaction. This NBA model was also good at flux reconstruction, but was not markedly better than our FBA method. However, the NBA cannot be used to reconstruct fluxes underlying experimental sparks because it requires the (nonobservable) calcium-free fluo-3 as input. We have overcome this limitation with the novel PFA, a fitting algorithm that uses the full binding model (including dye–protein binding kinetics) and is also less sensitive to noise in the input data.

Flux reconstruction from average sparks

Ca^{2+} flux reconstruction from individual experimental sparks records is problematic due to the generally low signal-to-noise ratio. Averaging spark records provides, in principle, a useful way to improve the signal-to-noise ratio. Because the FBA contains nonlinear steps (e.g., Eq. A13) it was necessary to show that the FBA behaved linearly with respect to averaging, and that this was the case was demonstrated in Fig. 7. We electrically evoked sparks and selected well-separated, repeatedly firing spark sites. To obtain such well-defined sites, the probability of Ca^{2+} spark occurrence is reduced by a Ca^{2+} channel blocker, such as nifedipine, which does not alter the properties of Ca^{2+} sparks (Collier et al., 1999). In addition, sites chosen for averaging must not be contaminated by release events from nearby sites; this strict criterion resulted in <10% of experiments yielding sites for further analysis. Furthermore, we viewed it to be important to select sparks that were at least as large ($F/F_0 > 2.5$) as the average spark amplitude to ensure that the site was close to the line scanned by the confocal microscope (Pratusevich and Balke, 1996; Izu et al., 1998; Cheng et al., 1999). From consideration of our selection criteria (selecting from the brightest 25% of sparks), we estimate that the sparks analyzed here should have been, on average, ~0.25 μm from the scan line (Izu et al., 1998). We therefore predict that we underestimate the true current amplitude by a factor of ~1.4 (see Fig. 5 *B*). In contrast, sparks have been shown to be larger in the longitudinal direction by ~18% (Cheng et al., 1996b). Because we recorded sparks in the longitudinal direction and assumed a spherical fluorescence distribution, we would have overestimated the current by a volume factor of 1.18^2 or ~1.4. This analysis suggests that these two effects, taken together, compensate each other, and our calculated current amplitudes should be a reasonable estimate of the underlying release fluxes.

By averaging >9 individual Ca^{2+} sparks, the improved signal-to-noise ratio allowed the FBA and the PFA to produce an estimate of the amplitude and time course of the Ca^{2+} release flux underlying these sparks. The FBA and PFA reconstructed release current time courses were similar with regard to rise time (4–5 ms) and peak amplitude (7–12 pA). Although the currents calculated with the PFA decayed approximately exponentially, the traces calculated with the FBA seemed to terminate more abruptly. We suggest that this can be largely explained by the noise sensitivity of the FBA because we observed a similar effect when the FBA was used to reconstruct a noisy simulated spark arising from an exponentially decaying release waveform (Fig. 6 *B*).

Comparison of the release time course of the three average sparks that were analyzed suggested that the decay times were very similar, although the amplitudes of these three sparks were quite different (Fig. 10 *A*), in contrast to the results by Lukyanenko et al. (1998).

It is also important to note that our spark model reproduces the spatial dimension of Ca^{2+} sparks, which has been a deficiency in all previous spark models. This improvement was achieved by allowing the region of release to grow with time during the period of release. Such an effect could be reasonably explained by recruitment of RyRs from the site of initiation during the early phase of a spark evolution. Indeed, electron micrographs of couplons show them to be quite extended (Franzini-Armstrong et al., 1999).

It is notable that the SR release flux of 7–12 pA is more than twice as large as that estimated by Cheng et al. (1993) and Blatter et al. (1997). When comparing local flux densities, our estimate of ~50 mM/s is five times larger than that reported by Blatter et al. (1997) and nearly an order of magnitude larger than that estimated by Lukyanenko et al. (1998). We suggest that the previous studies underestimate the fluxes underlying the spark for several reasons: 1) the use of extensive filtering to suppress noise (Lukyanenko et al., 1998); 2) the use of SBA-type approaches (Blatter et al., 1997; Lukyanenko et al., 1998); and 3) low values for the fluo-3 binding constants (Cheng et al., 1993; Blatter et al., 1997; Lukyanenko et al., 1998). In a recent study that sought to explain the spatial dimensions of Ca^{2+} sparks, a lower estimate of ~11 pA was obtained (Izu et al., 2001), which agrees reasonably with our estimates. However, the same study suggested that the current underlying a Ca^{2+} spark could be as large as ~40 pA, which would be associated with abnormal spark amplitudes ($F/F_0 \approx 12$). Our estimate is approximately five times larger than that estimated by calibrating spark amplitude with local fluorescence changes produced by dihydropyridine receptor (DHPR) gating (Wang et al., 2001). A part of this difference resides in the spark amplitudes being larger in our experiments. Additionally, it is possible that the site from which the DHPR current was recorded was some distance from the spark site in the experiments of Wang et al. (2001). This idea is supported by their observation of an abnormally long delay between DHPR opening and spark activation and a relatively low coupling efficiency, despite the (drug-induced) long DHPR open times in their study.

Given an SR release flux of >7.5 pA, we can estimate that at least ~15 RyRs must be activated during a Ca^{2+} spark (for a single RyR current of ~0.5 pA, Mejia-Alvarez et al., 1999). Because this cluster of RyRs opens within ~4 ms, we can estimate that the opening rate constant must be ~500/s (if 4 ms equals two time constants) which, if Ca^{2+} gated, implies a local trigger level of ~10 μM for a diffusion-limited on rate of $2 \times 10^8\ M^{-1}s^{-1}$. This estimate of the local trigger Ca^{2+} is in good agreement with previous detailed mathematical modeling of the dyadic cleft (Cannell and Soeller, 1997; Soeller and Cannell, 1997) and an analysis of the increase in spark rate during excitation–contraction coupling (Cannell et al., 1994). By examining ruthenium red inhibition of RyRs it was estimated that >10 RyRs should be involved in a Ca^{2+} spark (Lukyanenko et al., 2000). Using a different approach, Bridge et al. (1999) estimated that at least 19 RyRs were activated during a Ca^{2+} spark, in reasonable agreement with our results. To achieve the activation of ~15 RyRs within the dyadic release units (couplons) places some constraints on the relationship between the open probability P_o of the RyRs and the number present. For example, electron microscopic measurements estimate that there are ~100 RyRs in couplons in mammalian cardiac muscle (Franzini-Armstrong et al., 1999), suggesting that $P_o \geq 0.15$. For 100 RyRs, such a P_o would be associated with significant flux noise, if the RyRs gated independently. For a mean of 15 RyRs with a P_o of 0.15, the standard deviation in the number open is 3.6 (Bridge et al., 1999). Therefore, 95% of the time between 8 and 22 channels would be open, which would equate to a more than two-fold variation in flux during the rising phase of a spark. A second consequence of such a large flux variation associated with independent gating would be a large variation in the duration of the release flux. Inasmuch as we do not observe such a large variation in sparks at a fixed site (cf. Fig. 8 *B*) we suggest that it is likely that RyRs are functionally coupled. Such coupling could be explained by RyR gating being conformationally coupled (Marx et al., 2001) or by the Ca^{2+} flux via one or more RyRs influencing the Ca^{2+} flux through adjacent RyRs (by affecting local SR luminal Ca^{2+}) and the indirect coupling of RyRs via the local $[Ca^{2+}]$ in the cleft.

Finally, although our flux determination includes the sarcolemmal trigger Ca^{2+} flux, this component should be no more than ~10% of the SR release flux. This has been demonstrated by a number of experimental and theoretical analyses (e.g., Cannell et al., 1987; Sipido and Wier, 1991; Rice et al., 1999). In conclusion, we have shown that, by incorporating signal averaging with novel flux reconstruction algorithms, it is possible to provide reliable estimates of the fluxes underlying local Ca^{2+} signals. The approaches we present should be generally applicable to any model cell system.

APPENDIX A

Flux reconstruction in the presence of reversible dye binding

The equations for Ca^{2+} release flux reconstruction are obtained by starting from the partial differential equations that describe the spatio-temporal evolution of Ca^{2+}, the various indicator species and the other Ca^{2+} buffers and uptake systems in the cytosol (Blatter et al., 1997; Lukyanenko et al., 1998; Rios et al., 1999). Using the reversible indicator binding scheme

shown in Fig. 3 *A*, the evolution of the freely diffusing fluo3–Ca complex (F3Ca) is governed by

$$\frac{\partial[\mathrm{F3Ca}]}{\partial t} = k_{on}^{F3}[\mathrm{F3}][Ca^{2+}] - k_{off}^{F3}[\mathrm{F3Ca}] + D_{F3}\Delta[\mathrm{F3Ca}] + k_{off}^{PCa}[\mathrm{PF3Ca}] - k_{on}^{PCa}[\mathrm{F3Ca}][\mathrm{P}], \quad (A1)$$

and similarly for the protein-bound fluo3–Ca complex (PF3Ca)

$$\frac{\partial[\mathrm{PF3Ca}]}{\partial t} = k_{on}^{PF3}[\mathrm{PF3}][Ca^{2+}] - k_{off}^{PF3}[\mathrm{PF3Ca}] - k_{off}^{PCa}[\mathrm{PF3Ca}] + k_{on}^{PCa}[\mathrm{F3Ca}][\mathrm{P}]. \quad (A2)$$

Adding those two equations and introducing the total Ca-bound dye,

$$[\mathrm{TF3Ca}] = [\mathrm{F3Ca}] + [\mathrm{PF3Ca}], \quad (A3)$$

one can solve for the free Ca^{2+} concentration,

$$[Ca^{2+}] = \frac{\frac{\partial}{\partial t}[\mathrm{TF3Ca}] + k_{off}^{F3}[\mathrm{F3Ca}] + k_{off}^{PF3}[\mathrm{PF3Ca}] - D_{F3}\Delta[\mathrm{F3Ca}]}{k_{on}^{F3}[\mathrm{F3}] + k_{on}^{PF3}[\mathrm{PF3}]}. \quad (A4)$$

Using this equation, $[Ca^{2+}]$ can be computed from (measured) concentrations of freely diffusing (F3Ca and F3) and protein bound (PF3Ca and PF3) fluo3/fluo3–Ca complex. The SR Ca^{2+} release flux q_{Ca} can now be obtained in a similar way starting from the equation of evolution of $[Ca^{2+}]$.

$$\frac{\partial[Ca^{2+}]}{\partial t} = q_{Ca} + k_{off}^{F3}[\mathrm{F3Ca}] + k_{off}^{PF3}[\mathrm{PF3Ca}] - (k_{on}^{F3}[\mathrm{F3}] + k_{on}^{PF3}[\mathrm{PF3}])[Ca^{2+}] + q_{buf} + q_{rem} + D_{Ca}\Delta[Ca^{2+}], \quad (A5)$$

where q_{rem} is the removal flux due to SR uptake and q_{buf} denotes the Ca^{2+} movements onto and off endogenous Ca^{2+} buffer species B_i

$$q_{buf} = \sum_i q_i = \sum_i k_{off}^{i}[\mathrm{B_iCa}] - k_{on}^{i}[\mathrm{B_i}][Ca^{2+}], \quad (A6)$$

where q_i is the movement due to buffer species B_i, and k_{off}^{i} and k_{on}^{i} are the corresponding off and on-rates, respectively. Rearranging Eqs. A5 and using A4, the release flux is obtained

$$q_{Ca} = \frac{\partial[Ca^{2+}]}{\partial t} + \frac{\partial[\mathrm{TF3Ca}]}{\partial t} - D_{Ca}\Delta[Ca^{2+}] - D_{F3}\Delta[\mathrm{F3Ca}] - q_{buf} - q_{rem}. \quad (A7)$$

Required input data are again the measured concentrations of the various fluo3/fluo3–Ca species and additionally the previously computed Ca^{2+} distribution. The buffer fluxes q_i can be calculated by integration of the equations of evolution of the relevant buffer species in time (using the $[Ca^{2+}]$ calculated from Eq. A4),

$$\frac{\partial}{\partial t}B_i = k_{off}^{i}[\mathrm{B_iCa}] - k_{on}^{i}[Ca^{2+}][\mathrm{B_i}] + D_i\Delta\mathrm{B_i}, \quad (A8)$$

where D_i is the diffusion coefficient of buffer species B_i. The removal flux q_{rem} can be obtained from the calculated $[Ca^{2+}]$ and the model of the SR uptake process (see Methods).

The equations for the simple binding model (SBA, see Methods) are special cases of Eqs. A4 and A7 in which [P], [PF3Ca], and [PF3] are set to zero and the lower apparent diffusion coefficient $D_{F3,app}$ is used. The resulting equations are

$$[Ca^{2+}] = \frac{\frac{\partial}{\partial t}[\mathrm{F3Ca}] + k_{off}^{F3}[\mathrm{F3Ca}] - D_{F3,app}\Delta[\mathrm{F3Ca}]}{k_{on}^{F3}(\mathrm{F3_T} - [\mathrm{F3Ca}])}, \quad (A9)$$

$$q_{Ca} = \frac{\partial[Ca^{2+}]}{\partial t} + \frac{\partial[\mathrm{F3Ca}]}{\partial t} - D_{Ca}\Delta[Ca^{2+}] - D_{F3,app}\Delta[\mathrm{F3Ca}] - q_{buf} - q_{rem}. \quad (A10)$$

The fast binding approximation

If the binding of fluo-3 to proteins is instantaneous knowledge of the total fluorescence signal (which is proportional to TF3Ca) is sufficient to compute q_{Ca}. In the following, the approach outlined in the previous section is modified accordingly to derive the equations of the FBA. First, we introduce the ratios of protein bound to free fluo3/fluo-3–Ca complex,

$$c_f = \frac{[\mathrm{PF3}]}{[\mathrm{F3}]} = \frac{1}{1 + k_{off}^{P}/k_{on}^{P}[\mathrm{P}]} \quad (A11)$$

and

$$c_{Ca} = \frac{[\mathrm{PF3Ca}]}{[\mathrm{F3Ca}]} = \frac{1}{1 + k_{off}^{PCa}/k_{on}^{PCa}[\mathrm{P}]}. \quad (A12)$$

In principle c_f and c_{Ca} are Ca^{2+} dependent. This dependency, however, is very weak: c_f and c_{Ca} change by less than 1% as $[Ca^{2+}]$ is varied from 0.1 μM to 10 mM. In the approximation of the FBA, c_{Ca} and c_f are therefore regarded as constant (the values calculated at resting Ca^{2+} are used in the implementation). Using Eqs. A11 and A12, the quantities F3Ca, PF3Ca, and PF3 can be replaced by expressions only involving c_f, c_{Ca}, TF3Ca, and F3. Making these substitutions in Eq. A4, one obtains

$$[Ca^{2+}] = \frac{\frac{\partial}{\partial t}[\mathrm{TF3Ca}] + \frac{k_{off}^{eff}}{1 + c_{Ca}}[\mathrm{TF3Ca}] - \frac{D_{F3}}{1 + c_{Ca}}\Delta[\mathrm{TF3Ca}]}{k_{on}^{eff}[\mathrm{F3}]} \quad (A13)$$

where

$$k_{on}^{eff} = k_{on}^{F3} + c_f k_{on}^{PF3} \qquad k_{off}^{eff} = k_{off}^{F3} + c_{Ca}k_{off}^{PF3}. \quad (A14)$$

The only quantity in Eq. A13 that is not easily accessible to experimental observation is the concentration of freely diffusing fluo-3 ([F3]). Because

only part of the total fluo-3 is freely diffusing, [F3] cannot be obtained by simply relying on the local constancy of the total fluo-3 concentration ([F3 + F3Ca + PF3 + PF3Ca]). Instead, starting from the equation of evolution of the total dye concentration,

$$\frac{\partial[\mathrm{F3} + \mathrm{F3Ca} + \mathrm{PF3} + \mathrm{PF3Ca}]}{\partial t} = D_{\mathrm{F3}}\Delta[\mathrm{F3} + \mathrm{F3Ca}], \tag{A15}$$

which can be rearranged using Eqs. A11 and A12 to yield

$$\frac{\partial}{\partial t}\left([\mathrm{F3}] + \frac{[\mathrm{TF3Ca}]}{1 + c_{\mathrm{f}}}\right) = \frac{D_{\mathrm{F3}}}{1 + c_{\mathrm{f}}}\Delta\left([\mathrm{F3}] + \frac{[\mathrm{TF3Ca}]}{1 + c_{\mathrm{Ca}}}\right). \tag{A16}$$

Eq. A16 can be rewritten to obtain another diffusion equation for a "pseudo species" FF,

$$\frac{\partial}{\partial t}[\mathrm{FF}] = \frac{D_{\mathrm{F3}}}{1 + c_{\mathrm{f}}}\Delta[\mathrm{FF}] + Q, \tag{A17}$$

where

$$[\mathrm{FF}] = [\mathrm{F3}] + \frac{[\mathrm{TF3Ca}]}{1 + c_{\mathrm{f}}}, \tag{A18}$$

$$Q = D_{\mathrm{F3}}\frac{c_{\mathrm{f}} - c_{\mathrm{Ca}}}{(1 + c_{\mathrm{f}})^2(1 + c_{\mathrm{Ca}})}\Delta[\mathrm{TF3Ca}]. \tag{A19}$$

Eq. A17 can be integrated using the known source term Q (calculated via Eq. A19 from experimental data) to obtain the time course of FF. Using Eq. A18, we finally get the time course of [F3] that allows calculation of $[Ca^{2+}]$ according to Eq. A13.

Finally, the flux q_{Ca} can be computed if the identity below is used to replace [F3Ca] in Eq. A7 (with the approximation c_{Ca} = const, see above),

$$[\mathrm{F3Ca}] = \frac{[\mathrm{TF3Ca}]}{1 + c_{\mathrm{Ca}}}. \tag{A20}$$

The equations derived above were used in a three-step procedure to calculate the time course of Ca^{2+} release. In the initial step of the FBA, the total fluo-3–Ca complex distribution ([TF3Ca]) was calculated from the normalized fluorescence data (F/F_0) that was obtained by dividing the fluorescence transient by the resting fluorescence recorded before the spark. The total Ca^{2+}-bound fluo-3 is directly proportional to F/F_0 and was obtained by multiplication with the estimated resting TF3Ca concentration ($[\mathrm{TF3Ca}]_0$),

$$[\mathrm{TF3Ca}] = [\mathrm{TF3Ca}]_0 F/F_0. \tag{A21}$$

$[\mathrm{TF3Ca}]_0$ was calculated from the estimated resting Ca^{2+} (100 nM), the total fluo-3 concentration (100 μM), and the binding rates of the Harkins scheme (cf. Eqs. B1–B8).

In the second step of the FBA, the F3 distribution was calculated, because it is required to compute $[Ca^{2+}]$ (cf. Eq. A13). It was obtained by numerically integrating the diffusion equation A17 subject to the source term Q, which was computed by processing [TF3Ca] according to Eq. A19. The initial distribution of FF ($[\mathrm{FF}]_0$) was computed from Eq. A19,

$$[\mathrm{FF}]_0 = [\mathrm{F3}]_0 + \frac{[\mathrm{TF3Ca}]_0}{1 + c_{\mathrm{f}}}, \tag{A22}$$

where the initial values of $[\mathrm{F3}]_0$ and $[\mathrm{TF3Ca}]_0$ were determined from the Harkins scheme as suggested above. The resulting distribution of the pseudo species FF obtained from the numerical integration of Eq. A17 was transformed into the desired F3 distribution using Eq. A19. The freely diffusing Ca^{2+}-free fluo-3 ([F3]) and the total Ca^{2+}-bound fluo-3 distribution ([TF3Ca]) were then used to calculate $[Ca^{2+}]$ via Eq. A13.

In the third and final step, the Ca^{2+} release flux q_{Ca} was obtained from Eqs. A7 and A20 by differentiating the previously calculated [TF3Ca] and $[Ca^{2+}]$ (steps 1 and 2). Additionally, the fluxes q_{buf} and q_{rem} (due to Ca^{2+} buffering and SR uptake) are required for the calculation of q_{Ca} via Eq. A7. The buffer fluxes q_{buf} were calculated by numerically integrating Eq. A8 for the various buffer species using the previously determined $[Ca^{2+}]$. The SR uptake flux q_{rem} was directly obtained from Eq. 1 using the calculated $[Ca^{2+}]$ distribution.

The corresponding steps of the SBA were analogous but based on Eqs. A9, A10, and the simplified fluo-3 binding scheme (see Methods). The NBA included the full differential equations for protein binding but would not be suitable for experimental reconstruction because it is not possible to obtain an independent measure of protein bound and unbound F3Ca complex. Nevertheless, this algorithm was useful for testing reconstruction accuracy from realistic model Ca^{2+} sparks.

APPENDIX B

This appendix lists the equations to calculate the equilibrium distribution of the various species in the Harkins scheme. Given a total dye concentration ($\mathrm{F3_T}$), total dye-binding protein concentration ($\mathrm{P_T}$), a free $[Ca^{2+}]$ and the scheme shown in Fig. 3 *A*, first the total freely diffusing fluo-3 concentration ($\mathrm{FF3_T}$) is calculated. $\mathrm{FF3_T}$ was calculated by using the fact that, at equilibrium, all the local reactions are in equilibrium with each other.

$$\mathrm{FF3_T} = \frac{\mathrm{P_T} - \mathrm{F3_T} + K_{\mathrm{D}}^{\mathrm{eff}}}{2} + \sqrt{\frac{(\mathrm{P_T} - \mathrm{F3_T} + K_{\mathrm{D}}^{\mathrm{eff}})^2}{4} + K_{\mathrm{D}}^{\mathrm{eff}}\mathrm{F3_T}}, \tag{B1}$$

where

$$\mathrm{FF3_T} = [\mathrm{F3}] + [\mathrm{F3Ca}], \tag{B2}$$

and the effective binding constant $K_{\mathrm{D}}^{\mathrm{eff}}$ is

$$K_{\mathrm{D}}^{\mathrm{eff}} = \frac{k_{\mathrm{off}}^{\mathrm{eff}}}{k_{\mathrm{on}}^{\mathrm{eff}}} = \frac{k_{\mathrm{off}}^{\mathrm{p}} + \dfrac{k_{\mathrm{off}}^{\mathrm{PCa}}[Ca^{2+}]}{K_{\mathrm{D}}^{\mathrm{F3}}}}{1 + \dfrac{[Ca^{2+}]}{K_{\mathrm{D}}^{\mathrm{F3}}}}\,\frac{1 + \dfrac{[Ca^{2+}]}{K_{\mathrm{D}}^{\mathrm{PF3}}}}{k_{\mathrm{on}}^{\mathrm{p}} + \dfrac{k_{\mathrm{on}}^{\mathrm{PCa}}[Ca^{2+}]}{K_{\mathrm{D}}^{\mathrm{PF3}}}}. \tag{B3}$$

The previous equation uses the binding constants for protein-free and protein-bound fluo-3,

$$K_{\mathrm{D}}^{\mathrm{F3}} = \frac{k_{\mathrm{off}}^{\mathrm{F3}}}{k_{\mathrm{on}}^{\mathrm{F3}}}, \qquad K_{\mathrm{D}}^{\mathrm{PF3}} = \frac{k_{\mathrm{off}}^{\mathrm{PF3}}}{k_{\mathrm{on}}^{\mathrm{PF3}}}. \tag{B4}$$

From $\mathrm{FF3_T}$, all other quantities are readily obtained.

$$[\mathrm{PF3Ca}] = (\mathrm{F3_T} - \mathrm{FF3_T})\frac{1}{1 + K_{\mathrm{D}}^{\mathrm{PF3}}/[Ca^{2+}]}, \tag{B5}$$

$$[\mathrm{PF3}] = \mathrm{F3_T} - \mathrm{FF3_T} - [\mathrm{PF3Ca}], \tag{B6}$$

$$[\mathrm{F3Ca}] = \mathrm{FF3_T}\frac{1}{1 + K_{\mathrm{D}}^{\mathrm{F3}}/[Ca^{2+}]}, \tag{B7}$$

$$[\mathrm{F3}] = \mathrm{FF3_T} - [\mathrm{F3Ca}]. \tag{B8}$$

This work was supported by the Auckland Medical Research Foundation and the Health Research Council of New Zealand.

We would like to thank the reviewer for suggesting exploration of a model-fitting approach.

REFERENCES

Balke, C. W., T. M. Egan, and W. G. Wier. 1994. Processes that remove calcium from the cytoplasm during excitation–contraction coupling in intact rat heart cells. *J. Physiol.* 474:447–462.

Bassani, J. W., R. A. Bassani, and D. M. Bers. 1994. Relaxation in rabbit and rat cardiac cells: species-dependent differences in cellular mechanisms. *J. Physiol.* 476:279–293.

Baylor, S. M., and S. Hollingworth. 1998. Model of sarcomeric Ca^{2+} movements, including ATP Ca^{2+} binding and diffusion, during activation of frog skeletal muscle. *J. Gen. Physiol.* 112:297–316.

Blatter, L. A., J. Huser, and E. Rios. 1997. Sarcoplasmic reticulum Ca^{2+} release flux underlying Ca^{2+} sparks in cardiac muscle. *Proc. Natl. Acad. Sci. U.S.A.* 94:4176–4181.

Bridge, J. H., P. R. Ershler, and M. B. Cannell. 1999. Properties of Ca^{2+} sparks evoked by action potentials in mouse ventricular myocytes. *J. Physiol.* 518:469–478.

Bromba, M. U. A., and H. Ziegler. 1981. Application hints for Savitzky-Golay digital smoothing filters. *Anal. Chem.* 53:1583–1586.

Cannell, M. B., J. R. Berlin, and W. J. Lederer. 1987. Effect of membrane potential changes on the calcium transient in single rat cardiac muscle cells. *Science.* 238:1419–1423.

Cannell, M. B., H. Cheng, and W. J. Lederer. 1994. Spatial non-uniformities in $[Ca^{2+}]_i$ during excitation–contraction coupling in cardiac myocytes. *Biophys. J.* 67:1942–1956.

Cannell, M. B., H. Cheng, and W. J. Lederer. 1995. The control of calcium release in heart muscle. *Science.* 268:1045–1049.

Cannell, M. B., and C. Soeller. 1997. Numerical analysis of ryanodine receptor activation by L-type channel activity in the cardiac muscle diad. *Biophys. J.* 73:112–122.

Cannell, M. B., and C. Soeller. 1998. Local control in calcium signalling during cardiac E–C coupling. *In* Integrative Aspects of Calcium Signalling. A. Verkhratsky and E. C. Toescu, editors. Plenum Press, New York. 381–398.

Chance, E. M., A. R. Curtis, I. P. Jones, and C. R. Kirby. 1977. FACSIMILE: a computer program for flow and chemistry simulation, and general initial value problems. Computer Science and Systems Division, AERE Harwell, Oxfords. HMSO, London, UK.

Cheng, H., M. R. Lederer, W. J. Lederer, and M. B. Cannell. 1996a. Calcium sparks and $[Ca^{2+}]_i$ waves in cardiac myocytes. *Am. J. Physiol. Cell Physiol.* 270:C148–C159.

Cheng, H., M. R. Lederer, R. P. Xiao, A. M. Gomez, Y. Y. Zhou, B. Ziman, H. Spurgeon, E. G. Lakatta, and W. J. Lederer. 1996b. Excitation–contraction coupling in heart: new insights from Ca^{2+} sparks. *Cell Calcium.* 20:129–140.

Cheng, H., W. J. Lederer, and M. B. Cannell. 1993. Calcium sparks: elementary events underlying excitation–contraction coupling in heart muscle. *Science.* 262:740–744.

Cheng, H., L. S. Song, N. Shirokova, A. Gonzalez, E. G. Lakatta, E. Rios, and M. D. Stern. 1999. Amplitude distribution of calcium sparks in confocal images: theory and studies with an automatic detection method. *Biophys. J.* 76:606–617.

Collier, M. L., A. P. Thomas, and J. R. Berlin. 1999. Relationship between L-type Ca^{2+} current and unitary sarcoplasmic reticulum Ca^{2+} release events in rat ventricular myocytes. *J. Physiol.* 516:117–128.

Escobar, A. L., P. Velez, A. M. Kim, F. Cifuentes, M. Fill, and J. L. Vergara. 1997. Kinetic properties of DM-nitrophen and calcium indicators: rapid transient response to flash photolysis. *Pflugers Arch.* 434:615–631.

Evans, A. M., and M. B. Cannell. 1997. The role of L-type Ca^{2+} current and Na^+ current-stimulated Na/Ca exchange in triggering SR calcium release in guinea-pig cardiac ventricular myocytes. *Cardiovasc. Res.* 35:294–302.

Franzini-Armstrong, C., F. Protasi, and V. Ramesh. 1999. Shape, size, and distribution of Ca(2+) release units and couplons in skeletal and cardiac muscles. *Biophys. J.* 77:1528–1539.

Harkins, A. B., N. Kurebayashi, and S. M. Baylor. 1993. Resting myoplasmic free calcium in frog skeletal muscle fibers estimated with fluo-3. *Biophys. J.* 65:865–881.

Hollingworth, S., C. Soeller, S. M. Baylor, and M. B. Cannell. 2000. Sarcomeric Ca^{2+} gradients during activation of frog skeletal muscle fibres imaged with confocal and two-photon microscopy. *J. Physiol.* 526:551–560.

Izu, L. T., J. R. Mauban, C. W. Balke, and W. G. Wier. 2001. Large currents generate cardiac Ca^{2+} sparks. *Biophys. J.* 80:88–102.

Izu, L. T., W. G. Wier, and C. W. Balke. 1998. Theoretical analysis of the Ca^{2+} spark amplitude distribution. *Biophys. J.* 75:1144–1162.

Jorgensen, A. O., A. C. Shen, W. Arnold, P. S. McPherson, and K. P. Campbell. 1993. The Ca^{2+}-release channel/ryanodine receptor is localized in junctional and corbular sarcoplasmic reticulum in cardiac muscle. *J. Cell. Biol.* 120:969–980.

Kaplan, J. H., and G. C. Ellis-Davies. 1988. Photolabile chelators for the rapid photorelease of divalent cations. *Proc. Natl. Acad. Sci. U.S.A.* 85:6571–6575.

Klein, M. G., H. Cheng, L. F. Santana, Y. H. Jiang, W. J. Lederer, and M. F. Schneider. 1996. Two mechanisms of quantized calcium release in skeletal muscle. *Nature.* 379:455–458.

Ko, D. S., M. Sauer, S. Nord, R. Müller, and J. Wolfrum. 1997. Determination of the diffusion coefficient of dye in solution at single molecule level. *Chem. Phys. Lett.* 269:54–58.

Kushmerick, M. J., and R. J. Podolsky. 1969. Ionic mobility in muscle cells. *Science.* 166:1297–1298.

Langer, G. A., and A. Peskoff. 1996. Calcium concentration and movement in the diadic cleft space of the cardiac ventricular cell. *Biophys. J.* 70:1169–1182.

Luby-Phelps, K., M. Hori, J. M. Phelps, and D. Won. 1995. Ca(2+)-regulated dynamic compartmentalization of calmodulin in living smooth muscle cells. *J. Biol. Chem.* 270:21532–21538.

Lukyanenko, V., I. Gyorke, S. Subramanian, A. Smirnov, T. F. Wiesner, and S. Gyorke. 2000. Inhibition of Ca(2+) sparks by ruthenium red in permeabilized rat ventricular myocytes. *Biophys. J.* 79:1273–1284.

Lukyanenko, V., T. F. Wiesner, and S. Gyorke. 1998. Termination of Ca^{2+} release during Ca^{2+} sparks in rat ventricular myocytes. *J. Physiol.* 507:667–677.

Marx, S. O., J. Gaburjakova, M. Gaburjakova, C. Henrikson, K. Ondrias, and A. R. Marks. 2001. Coupled gating between cardiac calcium release channels (ryanodine receptors). *Circ. Res.* 88:1151–1158.

Mejia-Alvarez, R., C. Kettlun, E. Rios, M. Stern, and M. Fill. 1999. Unitary Ca^{2+} current through cardiac ryanodine receptor channels under quasi-physiological ionic conditions. *J. Gen. Physiol.* 113:177–186.

Parker, I., and W. G. Wier. 1997. Variability in frequency and characteristics of Ca^{2+} sparks at different release sites in rat ventricular myocytes. *J. Physiol.* 505:337–344.

Pratusevich, V. R., and C. W. Balke. 1996. Factors shaping the confocal image of the calcium spark in cardiac muscle cells. *Biophys. J.* 71: 2942–2957.

Press, W. H., S. A. Teukolsky, W. T. Vetterling, and B. P. Flannery. 1992. Numerical Recipes in C. Cambridge University Press, Cambridge, U.K. 650–655.

Rice, J. J., M. S. Jafri, and R. L. Winslow. 1999. Modeling gain and gradedness of Ca^{2+} release in the functional unit of the cardiac diadic space. *Biophys. J.* 77:1871–1884.

Rios, E., M. D. Stern, A. Gonzalez, G. Pizarro, and N. Shirokova. 1999. Calcium release flux underlying Ca^{2+} sparks of frog skeletal muscle. *J. Gen. Physiol.* 114:31–48.

Santana, L. F., H. Cheng, A. M. Gomez, M. B. Cannell, and W. J. Lederer. 1996. Relation between the sarcolemmal Ca^{2+} current and Ca^{2+} sparks and local control theories for cardiac excitation–contraction coupling. *Circ. Res.* 78:166–171.

Shacklock, P. S., W. G. Wier, and C. W. Balke. 1995. Local Ca^{2+} transients (Ca^{2+} sparks) originate at transverse tubules in rat heart cells. *J. Physiol.* 487:601–608.

Sipido, K. R., and W. G. Wier. 1991. Flux of Ca^{2+} across the sarcoplasmic reticulum of guinea-pig cardiac cells during excitation–contraction coupling. *J. Physiol.* 435:605–630.

Smith, G. D., J. E. Keizer, M. D. Stern, W. J. Lederer, and H. Cheng. 1998. A simple numerical model of calcium spark formation and detection in cardiac myocytes. *Biophys. J.* 75:15–32.

Soeller, C., and M. B. Cannell. 1997. Numerical simulation of local calcium movements during L-type calcium channel gating in the cardiac diad. *Biophys. J.* 73:97–111.

Soeller, C., and M. B. Cannell. 1999a. Examination of the transverse tubular system in living cardiac rat myocytes by 2-photon microscopy and digital image-processing techniques. *Circ. Res.* 84:266–275.

Soeller, C., and M. B. Cannell. 1999b. Two-photon microscopy: imaging in scattering samples and three-dimensionally resolved flash photolysis. *Microsc. Res. Tech.* 47:182–195.

Soeller, C., and M. B. Cannell. 2001. Modeling the Ca^{2+} spark and estimation of the SR Ca^{2+} release flux. *Biophys. J.* 80:63a.

Song, L. S., M. D. Stern, E. G. Lakatta, and H. Cheng. 1997. Partial depletion of sarcoplasmic reticulum calcium does not prevent calcium sparks in rat ventricular myocytes. *J. Physiol.* 505:665–675.

Stern, M. D. 1992. Theory of excitation–contraction coupling in cardiac muscle. *Biophys. J.* 63:497–517.

Tsugorka, A., E. Rios, and L. A. Blatter. 1995. Imaging elementary events of calcium release in skeletal muscle cells. *Science.* 269:1723–1726.

Wang, S. Q., L. S. Song, E. G. Lakatta, and H. Cheng. 2001. Ca^{2+} signalling between single L-type Ca^{2+} channels and ryanodine receptors in heart cells. *Nature.* 410:592–596.

Zhao, M., S. Hollingworth, and S. M. Baylor. 1996. Properties of tri- and tetracarboxylate Ca^{2+} indicators in frog skeletal muscle fibers. *Biophys. J.* 70:896–916.

Ziegler, H. 1981. Properties of digital smoothing polynomial (DISPO) filters. *Appl. Spectrosc.* 35:88–92.